

different chemical compositions of the basaltic intrusion and the tuff host rock; however, this level of detail was not attempted in this preliminary study. Fast kinetics were assumed with reaction rates close to local equilibrium. The value for the saturation cutoff used in the calculation was 0.001. Figure 11.4-20 shows the volume fraction of amorphous silica in the fracture at different times for the case of $\sigma_{fm} = 10^{-2}$. As the boiling front propagates into the host rock, silica precipitates from solution in the fractures. The source of silica is derived from the matrix upstream where dissolution of amorphous silica occurs (not shown). This result appears to be consistent with field observations at the Papoose Lake Sill.

11.4.7.3 Discussion

Although the field observations for mineral alteration are not inconsistent with the dual-continuum model predictions, there still remain a number of puzzling features. First, the close confinement of the alteration of the tuff host rock to zones adjacent to the intrusion is difficult to understand. This is the region that would be expected to be dry over the long term until the system cooled and rewetting took place. Whether the alteration could have occurred during the relatively rapid and transient passage of the boiling front as it swept through the host rock is still unresolved. It would appear difficult, however, to explain the extent of alteration of the matrix as caused by such a short-duration, transient event. Unfortunately, alteration of the matrix is not properly described by the dual-continuum connected-matrix model used here. A better approach would appear to be the dual-continuum disconnected-matrix formulation, which was beyond the scope of the present study.

A second puzzling feature is the sporadic appearance of alteration along the contact rather than a more uniform appearance, as modeling would predict. This feature could have several explanations. One is that nucleation kinetics were involved, and in most places, the reactions simply did not take place, although they were thermodynamically favored. This could be a result of low permeability and porosity values present in portions of the tuff (especially those that were fused) which would thus restrict the amount of water that could interact with the rock. Another possibility is that dehydration reactions of the basaltic dike released volatiles that reacted with the tuff host rock. Additionally, the host tuff may have had variable physical and chemical properties prior to the intrusion of the sill that might have resulted in non-uniform alteration.

Sensitivity analyses would help improve future models of the Paiute Ridge system. A number of the model input parameters are uncertain, and a sensitivity analysis would be useful to determine which parameters have the most impact on model results. In this regard, it should be emphasized that, for example, the van Genuchten parameters used for the intrusion and tuff country rock were not based on field measurement but were generic values that are approximate at best. The initial saturation condition of the tuff host rock plays an important role in moisture and heat redistribution, but is difficult, if not impossible, to know saturation values at the time the intrusion was emplaced.

11.4.8 Conclusions of Paiute Ridge Study

Magmatic intrusions in tuffaceous rock above the water table offer a unique opportunity to study conditions analogous to the potential Yucca Mountain high-level nuclear waste repository following emplacement of waste. The Paiute Ridge intrusive complex in partially saturated tuff

appears to offer a possible natural analogue site. A new result of this study is that the Papoose Lake Sill apparently intruded into Rainier Mesa tuff, and the resulting hydrothermal process was characterized by low-temperature alteration of glass to clinoptilolite and opal. The key observations of this study suggest that:

- The intrusion generally occurred at shallow levels and decreased in depth away from the central intrusive complex.
- The basalt along the contact is sheeted into narrow vertically or horizontally jointed plates, depending on whether the host tuff is exposed adjacent to or beneath the sill.
- Variable cooling patterns (e.g., glassy or crystallized fused tuff) occurred as noted along the intrusive contact.
- Alteration of nonwelded tuff to clinoptilolite and opal is similar to that observed in diagenetic processes at Yucca Mountain.
- Fractured zones in the tuff created by the basaltic intrusion were sealed by extensive silica remobilization during hydrothermal processes, resulting in low-porosity, highly indurated tuffs adjacent to the intrusive body.
- Hydrothermal alteration was confined to a narrow zone close to the contact zone, as indicated by major and trace element chemical data.

Field observations at the Paiute Ridge intrusive complex and results from laboratory analysis of altered and unaltered tuffs illustrate the intensity of hydrothermal alteration and extent of THC processes associated with thermal perturbation of rhyolitic ash flow tuffs. The secondary mineral assemblages are similar to those present at Yucca Mountain, and the presence of these minerals in the tuff at Paiute Ridge indicates the extent of the alteration. The pervasive anastomosing opal veins and associated secondary minerals (e.g., clinoptilolite, calcite, cristobalite) appear to have reduced matrix or fracture permeability in the immediate vicinity of the basaltic intrusion. The observed mineral zonations can be used to evaluate coupled process models. The widespread opal veins along fracture-matrix margins provide a means for evaluating porosity/permeability relationships and descriptions of fracture-matrix interaction employed in THC codes.

Preliminary results were presented for a one-dimensional THC dual-continuum model of the interaction of country rock with heat released from an intrusive complex emplaced above the water table. A simplified chemical system was considered involving precipitation and dissolution of amorphous silica. Results demonstrated the possibility of forming opal-filled veins with the source of silica derived from the matrix of the host rock. However, because of the irregularities caused by kinetic barrier effects associated with reaction of glass, it is important to compare and contrast a number of different natural analogue sites to be able to derive general conclusions regarding mineral alteration and, specifically, the effect of heat generated by a potential repository in tuff at Yucca Mountain.

Finally, an unexplained observation of this study is the proximal confinement of alteration of the tuff host rock to the intrusion. Additional modeling studies, and analytical data such as isotopes,

would elucidate the mechanisms responsible for the observed alteration patterns. A more extensive treatment of chemical processes, combined with the dual-continuum disconnected matrix formulation of the dual-continuum model, would allow for discretization of the rock matrix, thus resulting in more representative simulation results.

11.5 ANALOGUES TO THC EFFECTS ON TRANSPORT

The Marysville hydrothermal uranium-molybdenum ore deposit in Utah has been evaluated as a natural analogue for evaluating the effects of water-rock interaction and radionuclide transport. Depletions in igneous rock $\delta^{18}\text{O}$ values were interpreted to result from exchange with circulating meteoric waters (Shea and Foland 1986 [156672], p. 281). The largest ^{18}O depletions were observed along an intrusive contact, where enhanced fluid flow was thought to have occurred. Uranium mineralization related to the hydrothermal event associated with the intrusion appears to be concentrated along faults and fractures (Shea 1984 [156673], p. 327). Uranium is primarily concentrated in uranium-bearing mineral phases, such as uraninite and coffinite, but is also found associated with sericite and chlorite along zones of microfracturing. The observed distribution of uranium was interpreted to be due to both bulk-flow and diffusion-transport processes, with most transport (and subsequent deposition) occurring within the fracture network.

Wollenberg et al. (1995 [157467]) used gamma-ray spectrometry and fission-track radiography to examine the location and abundance of uranium and thorium in tuffaceous rocks encompassing hydrothermal systems at the Long Valley caldera, California, and the Valles caldera, New Mexico. In the lateral flowing hydrothermal system at the Long Valley caldera, where temperatures range from 140–200°C, uranium is concentrated to 50 ppm with Fe-rich mineral phases in brecciated tuff fragments. In the vapor zone of the Valles caldera's hydrothermal system (temperature ~100°C), the concordance of high uranium, low Th/U, and decreasing whole-rock oxygen-isotope ratios suggests that uranium was concentrated in response to hydrothermal circulation when the system was formerly liquid-dominated. In the underlying present-day liquid-dominated zone (temperature to 210°C), up to several tens of parts per million uranium occurs with pyrite and Fe-oxide minerals, and in concentrations to several percent with a Ti-Nb-Y rare-earth mineral.

In the Valles caldera's outflow zone, uranium is also concentrated in Fe-rich zones, as well as in carbonaceous-rich zones in the Paleozoic bedrock that underlies the Quaternary tuff. Thorium, associated with accessory minerals, predominates in breccia zones and in a mineralized fault zone near the base of the Paleozoic sedimentary sequence. Relatively high concentrations of uranium occur in springs representative of water recharging the Valles caldera's hydrothermal system. By contrast, considerably lower uranium concentrations occur in hot waters (>220°C) and in the system's outflow plume, suggesting that uranium is being concentrated in the hotter part of the system. The Long Valley and Valles observations indicate that uranium and radium are locally mobile under hydrothermal conditions, and that the reducing conditions associated with Fe-rich minerals and carbonaceous material are important factors in the adsorption of uranium and its attenuation in water at elevated temperature. The Valles and Long Valley studies provide evidence for at least localized mobility of uranium and its daughters in tuff and underlying sedimentary rocks at temperatures comparable to those expected in a nuclear waste repository environment.

11.6 ANALOGUES TO THM EFFECTS

11.6.1 Insights from Field Tests

Results of heater tests conducted at the NTS in granite and tuff and at the Stripa Swedish underground laboratory in granite showed a decrease in fracture permeability as a result of thermal expansion. The Climax spent fuel test at the NTS was conducted in a 426 m deep shaft in granite. During the three-year test, temperatures in the monitored region of the rock mass reached 80°C (Hardin and Chesnut 1998 [150043], pp. 4-1 to 4-3). No significant changes in mineralogy or microfracturing occurred as a result of heat or irradiation. Monitored permanent displacements were on the order of 0.1–1 mm (Hardin and Chesnut 1998 [150043], p. 4-3). The sense of displacement was consistent with the regional extensional tectonic regime.

Four heater experiments were conducted in G-tunnel, within Rainier Mesa, NTS. In the heated-block test, rock-mass mechanical and thermomechanical properties were measured in tuff under controlled thermal and stress-loading conditions. The block was subjected to maximum temperatures ranging from 76–145°C, and equal biaxial stresses with magnitudes up to 10.6 MPa (Zimmerman et al. 1986 [138273], pp. vii–ix). The permeability of a single, near-vertical fracture was measured. The largest changes in permeability were associated with excavation of the block, when the apparent permeability increased from 76 to 758 microdarcies. Subsequent compressive loading decreased the permeability but did not completely reverse the unloading conditions, and the apparent permeability ranged from 252–332 microdarcies over a stress range of 3.1–10.6 MPa (Hardin and Chesnut 1998 [150043], p. 4-6). Increased temperature under biaxial confinement decreased the fracture aperture, lowering the apparent permeability from 234 to 89 microdarcies during heating.

In addition to full-scale heater tests that investigated short-term near-field effects from thermal loading, a time-scaled heater test was also performed at the Stripa underground laboratory to investigate the long-term thermomechanical response to thermal loading (Robinson 1985 [157445]). In the full-scale and time-scale heater tests, heat flow was not affected by fractures or other discontinuities in the granitic rock mass. Thermoelastic deformation of the rock mass was nonlinear and less than predicted. Fracture closure in response to thermal expansion was confirmed by observation of diminished water inflow to the heater and instrument boreholes (Nelson et al. 1981 [150092], pp. 78–80) and by increased compressional wave velocity during heating (King and Paulsson 1981 [157444], p. 699).

11.6.2 Krasnoyarsk

Krasnoyarsk-26 (K-26) is an underground facility in south-central Siberia where nuclear power has been generated by three underground reactors for approximately four decades, with a byproduct of weapons-grade plutonium. The power generated by these reactors is used to provide heat, electricity, and hot water for the city of Zheleznogorsk. Although K-26 differs from Yucca Mountain in geology and hydrologic regime, with K-26 located in saturated, fractured Archean-Proterozoic gneisses, it is the longest “heater test” on record, with a 40-year record of thermal measurements.

A schematic of the underground workings is shown in Figure 11.6-1. The depth of the underground workings has not been reported precisely, but is estimated to be at ~200–300 m below the surface in saturated bedrock (Gupalo 2001 [157471], p. 9). Large sources of heat are present in the P-2 and P-4 underground workings, where air temperatures reach 60–65°C (Gupalo 2001 [157471] p. 15). Based on temperatures measurements in 125 boreholes around the heat sources over 30 years, the dynamics of the rock-mass heating have been obtained. The maximum temperature of the rock is 63°C. The 30°C isotherm is established at a distance of 30 m from the heat sources (Gupalo 2001 [157471], pp. 52, 83).

Facilities at B-3 and B-4 were constructed for “technological works” in 1960, but they have not been used. This makes it possible to monitor coupled processes in both types of underground facilities, those that have and have not been impacted by heat. The dimensions of the chambers containing the heat source are approximately 20 m wide × 60 m long × 40 m in height (Gupalo 2001 [157471], pp. 24, 83; 1999 [157470], p. 9). All chambers have a 1.6 m thick concrete lining.

The geologic conditions of the P-2, P-4, B-3, and B-4 facilities are quite different. Chamber P-2 is located in the footwall of a steeply dipping zone of cataclasis and is surrounded by schistose zones. Chambers P-4 and B-4 are located in fractured gneiss (Gupalo 2001 [157471], p. 15).

The convergence of underground chamber walls as a result of manmade disturbances has been small over the 40-year lifetime of the facility. The largest values of convergence were measured in chamber P-2, where convergence ranged from 16.9–21.5 mm. In chamber P-4, maximum convergence of walls is half that of P-2. In B-4, maximum convergence of walls amounted to 1.55 mm, one order of magnitude less than the heated facilities in P-2 and P-4. Approximately similar heat sources operate in P-2 ($T = 45^{\circ}\text{C}$) and P-4 ($T = 62^{\circ}\text{C}$), such that their impact on the host rock is similar. The increased deformation in P-2, as compared to P-4, is attributed to the unfavorable mining and geologic conditions, compared to the rock mass in pillars surrounding chamber P-4 (Gupalo et al. 1999 [157470], p. 45).

According to the velocity of ultrasonic waves measured from logging seven boreholes, three zones of deformation can be distinguished in the rock mass: (1) a zone of concrete lining (0.0–1.6 m) and adjacent rock layer with high disturbance level (1.6–2.0 m); (2) a zone of contour rock layer of intermediate disturbance (1.6–2.0 m); (3) the undisturbed rock mass (over 4.0 m) (Gupalo et al. 1999 [157470], p. 80). The vertical component of convergence was determined to be 2.1 mm (+0.09 mm/yr from 1976 to 1998). (Gupalo 2001 [157471], p. 80).

The effect of thermal loads on rock-mass deformation was found to be significant in the disturbed zone. Within a homogeneous rock mass, convergence of chamber walls over a 40-year observation period was 1.0 mm in the absence of thermal impacts, but dislocations increased 8 to 10 times under increased temperature effects (Gupalo 2001 [157471], p. 81).

There is a clear temperature-related effect of the underground facilities on fracture-vein waters. The area of enhanced temperatures of underground water reaches 38–70 m above the roof of the workings, and maximum recorded temperatures of the underground waters is 36°C. (Gupalo 2001 [157471], p. 83).

Although the K-26 example is more analogous to preclosure conditions rather than postclosure performance at Yucca Mountain, it provides an example of relative thermomechanical stability under sub-boiling conditions in a more heterogeneous rock mass than that found at Yucca Mountain. It also provides a test case that compares a thermomechanically disturbed regime to one that is merely mechanically disturbed in the same rock mass, to determine the thermal component of disturbance.

11.6.3 THM Insights from Geothermal Fields

During the 1970s and 1980s, The Geysers geothermal region was rapidly developed as a site of geothermal power production. The likelihood that this could cause significant strain within the reservoir, with corresponding surface displacements, led to a series of deformation monitoring surveys from 1973 to 1996. For the period 1980-1994, peak volume strains occurred in excess of 5×10^{-4} . Changes in reservoir steam pressures were well correlated with volume strain and contraction of the reservoir (Mossop and Segall 1999 [157466], p. 29,113).

Seismicity has been induced by oil and gas production in areas where pore pressures have decreased, in some cases by several tens of MPa (Segall and Fitzgerald 1998 [157464], p. 117). Induced earthquakes are also common in geothermal fields, such as The Geysers, where strong correlations between earthquake activity and both steam production and condensate injection, have been observed. Stress measurements within hydrocarbon reservoirs show that the least horizontal stress decreases with declining reservoir pressure, as predicted by poroelasticity. Production-induced stressing may promote frictional sliding on pre-existing faults. However, it is not expected that this magnitude of stress would occur at Yucca Mountain.

Studies of hydraulic fracturing experiments in hot dry rock suggest that under thermal conditions, mechanical stresses in the rock at Yucca Mountain will occur along preexisting fracture zones and will develop in the direction of maximum principal stress. The Hijori hot dry rock site in Yamagata, Japan, was the site of hydraulic fracturing experiments in 1988 that were accompanied by microseismic events (Sasaki 1998 [157465], p. 171). The microseismic events were thought to have been caused by shear failures induced by high pore-fluid pressures occurring on planes of weakness in the rock surrounding the main hydraulic fracture. The experiment indicated a migration of the induced microseismic events that eventually distributed along a vertical plane, with the strike of seismicity nearly parallel to the direction of the maximum principal stress. The vertical orientation and east-west strike of the seismic events are essentially coplanar with the caldera ring-fault structure in the southern portion of the Hijori Caldera. This indicates that a preexisting fracture zone was being reopened and developed in the direction of maximum principal stress.

11.7 SUMMARY AND CONCLUSIONS

Geothermal systems illustrate a variety of THC processes that are relevant to Yucca Mountain. They include advective and conductive heating, fracture-dominated fluid flow, chemical transport, boiling and dryout, condensation, and mineral alteration, dissolution, and precipitation. Yellowstone and other geothermal systems in welded ash flow tuffs or other low-permeability rocks indicate that fluid flow is controlled by interconnected fractures. Alteration in low-permeability rocks is typically focused along fracture-flow pathways. Only a small portion of the

fracture volume needs to be sealed in order to retard fluid flow effectively. At Yucca Mountain, fluid flow and low-temperature water-rock interaction over the past 10 m.y. have resulted in the precipitation of minor amounts of opal and calcite on fracture and lithophysal cavity surfaces.

The main minerals predicted to precipitate in the near field of the potential Yucca Mountain repository are amorphous silica and calcite, which are also commonly found as sealing minerals in geothermal systems.

Sealing in geothermal fields can occur over a relatively short time frame (days to years). Precipitation of minerals can be triggered by a variety of processes, including boiling, water-rock interaction, heating and cooling of fluids, and fluid mixing. The unsaturated conditions, lower temperatures, and much lower fluid-flow rates predicted for the Yucca Mountain system in comparison to geothermal systems, should result in less extensive water-rock interaction than is observed in geothermal systems.

Fracturing and sealing occur episodically in geothermal systems. Different generations of fracture mineralization indicate that there are multiple pulses of fluid flow, recording distinct temperature conditions and fluid compositions, throughout the lifespan of a geothermal system. Most mineralization at Yucca Mountain is predicted to occur soon after waste emplacement (1,000–2,000 yr), when temperatures would reach boiling (for the higher-temperature operating mode) above the emplacement drifts.

The effects of processes such as boiling, condensation, dissolution, and precipitation on the higher-temperature operating mode for Yucca Mountain will be restricted to the near-field environment. Silica precipitation at Yellowstone results from both cooling and boiling processes, which serve to raise silica concentrations to above saturation levels. Geochemical modeling of fluid compositions has been used to successfully predict observed alteration of mineral assemblages at Yellowstone.

As shown in Section 11.3, THC processes are expected to have a much smaller effect on hydrogeological properties at Yucca Mountain than on those observed at Yellowstone. However, development of a heat pipe above emplacement drifts at Yucca Mountain under a higher-temperature operating mode could lead to increased chemical reaction and transport in the near field. Reflux and boiling of silica-bearing fluids within the near field at Yucca Mountain could cause fracture plugging, thus changing fluid-flow paths. THC simulations conducted to date for the potential Yucca Mountain repository suggest that only small reductions in fracture porosity (1–3%) and permeability (<1 order of magnitude) will occur in the near field as a result of amorphous silica and calcite precipitation (BSC 2001 [155950], Section 4.3.6.4.2). Changes in permeability, porosity, and sorptive capacity are expected to be relatively minor at the mountain scale, where thermal perturbations will be minimal; this also applies to the lower-temperature (sub-boiling) design. These predicted changes in hydrogeological properties should not significantly affect repository performance.

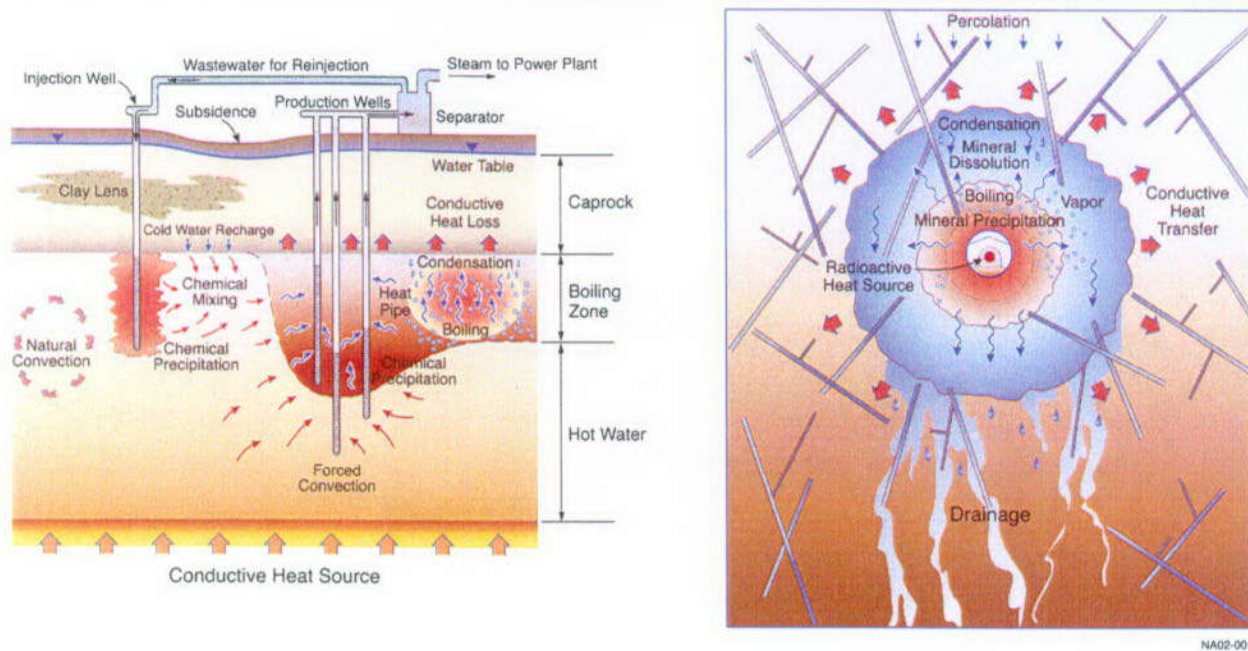
Magmatic intrusions in tuffaceous rock above the water table, such as the Paiute Ridge intrusive complex studied in Section 11.4, offer a unique opportunity to study conditions analogous to the predicted postclosure repository conditions at potential Yucca Mountain. The Papoose Lake Sill intruded into Rainier Mesa tuff, and the resulting hydrothermal effects were characterized by

low-temperature alteration of glass to clinoptilolite and opal, similar to those present at Yucca Mountain. Hydrothermal alteration was confined to a narrow zone close to the contact zone. The pervasive anastomosing opal veins and associated secondary minerals (e.g., clinoptilolite, calcite, cristobalite, etc.) appear to have reduced matrix or fracture permeability in the immediate vicinity of the basaltic intrusion.

The widespread opal veins along fracture-matrix margins provide a means for testing and validating porosity/permeability relationships and descriptions of fracture-matrix interaction employed in THC codes. Preliminary results of a one-dimensional THC dual-continuum model of the interaction of country rock with heat released from an intrusive complex emplaced above the water table demonstrated the possibility of forming opal-filled veins with the source of silica derived from the matrix of the host rock. However, because of the irregularities caused by kinetic barrier effects associated with the reaction of glass, it is important to compare and contrast a number of different sites to be able to derive general conclusions regarding mineral alteration and, specifically, the effect of heat generated by a potential repository in tuff at Yucca Mountain.

Examples provided in Section 11.5 indicate that the observed distribution of uranium resulting from hydrothermal conditions at Marysvale was a result of advective transport and diffusion, with most transport-subsequent precipitation of uranium occurring within the fracture network. This observation was also borne out at portions of the Long Valley and Valles calderas. The latter two studies also provided evidence for at least localized mobility of uranium-series radioisotopes at temperatures more comparable to those expected under higher-temperature thermal-loading conditions in a nuclear waste repository environment.

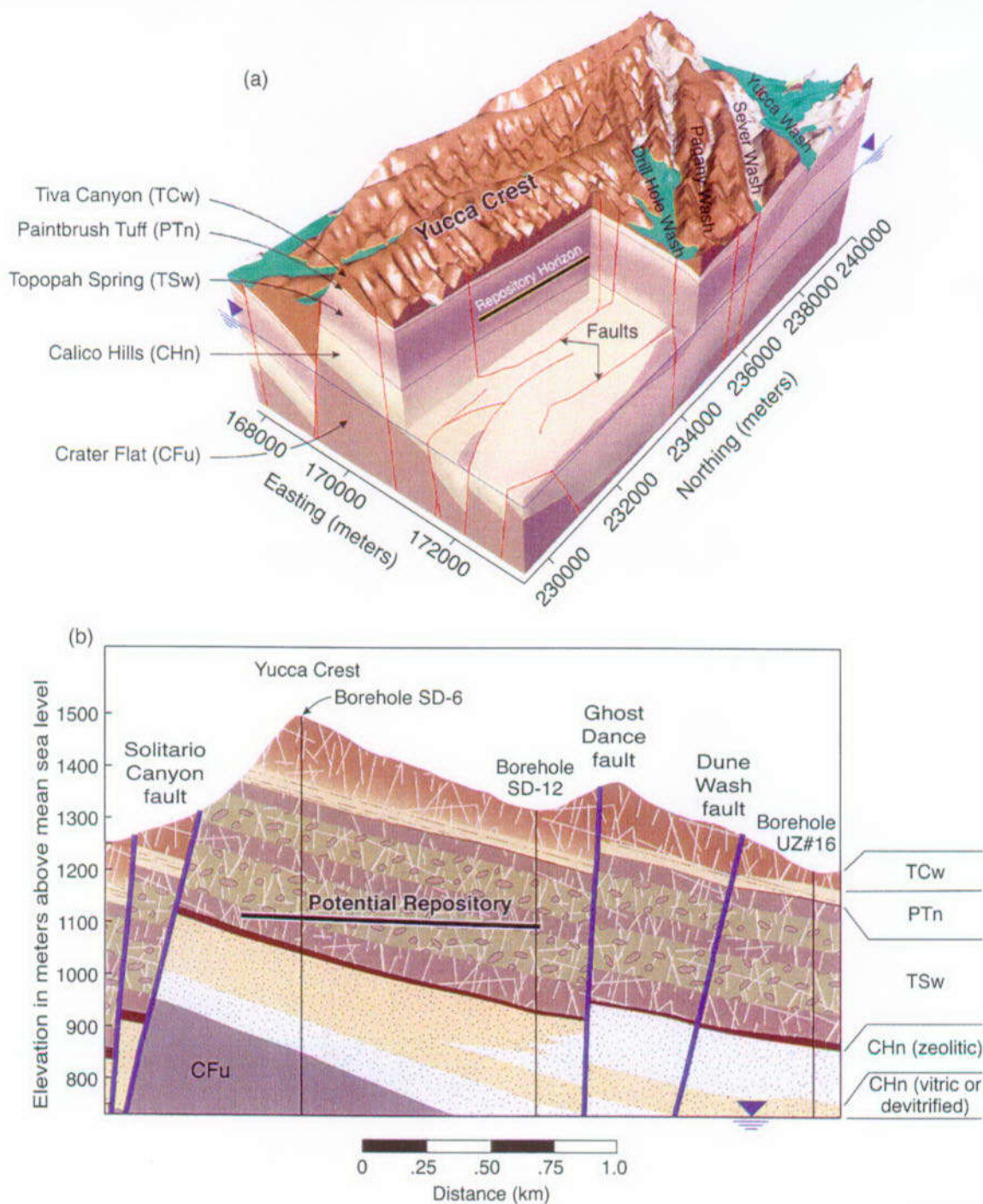
THM effects at Yucca Mountain (Section 11.6) are expected to be less extreme than those operating in geothermal fields where microseismicity is detected. Although rock type, hydrogeology, and design configurations differ from those at Yucca Mountain, the closest analogue identified so far is K-26, which is particularly relevant to lower-temperature design scenarios. Although the 40-year record of experiments should be interpreted cautiously with respect to extrapolation to long time periods, thermomechanical effects, such as drift convergence, might be in the same range of magnitude (on the order of a few mm) as that at Krasnoyarsk for the preclosure period.



NOTE: Similar processes include boiling and condensation, advective liquid flow, mineral dissolution and precipitation, mixing, recharge (percolation), and heat conduction. A heat pipe is depicted on the right side of the geothermal system, showing countercurrent liquid and vapor flow resulting from boiling and condensation.

Source: Left figure adapted from Bodvarsson and Witherspoon (1989 [156337]), right adapted from CRWMS M&O (2000 [151940]).

Figure 11.2-1. Comparison of Processes in Geothermal (Left) and Anthropogenic (Right) Thermal Systems Created by Emplacing Heat-Generating Nuclear Waste in an Unsaturated Fractured Rock Mass

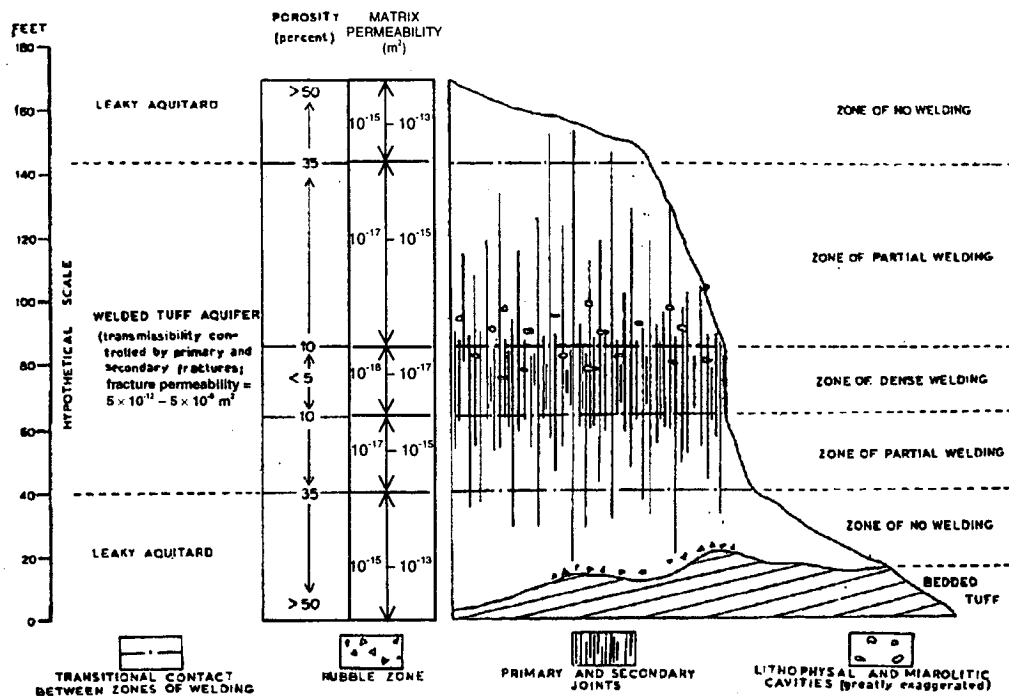


UZ02-002

NOTE: In both (a) and (b), the water table is indicated by a blue downward-pointing triangle.

Source: CRWMS M&O 2000 [151940], Figure 3.2-1.

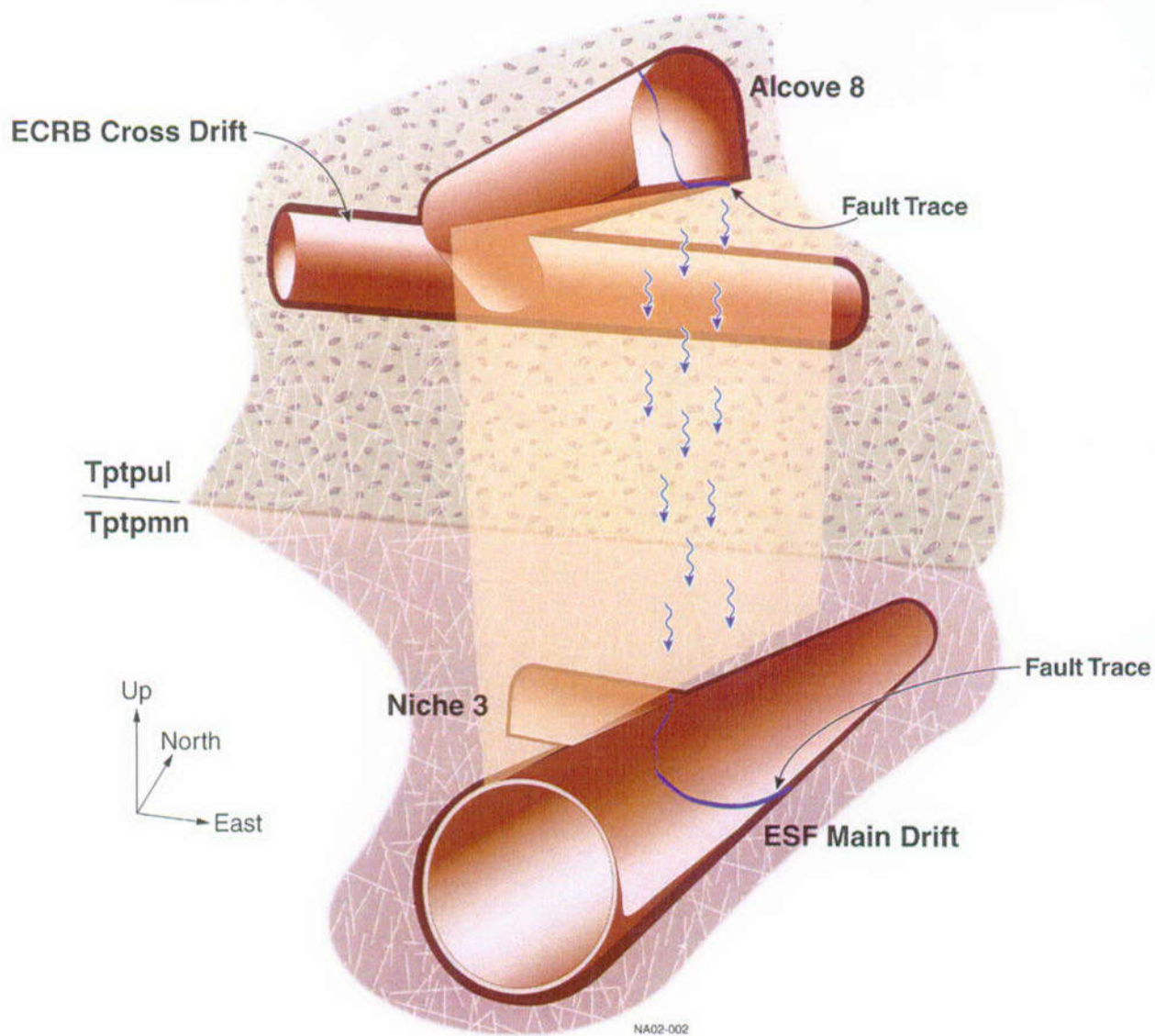
Figure 11.2-2. Schematic Diagram (a) and Cross Section (b) of the Yucca Mountain Lithology and Topography, Including Surface Features and Major Geologic Strata



NOTE: While zones of dense welding have intrinsically low matrix permeabilities, these zones also have much more abundant fractures, resulting in higher overall permeability than nonwelded (and unfractured) tuff.

Source: Generic profile modified from Winograd (1971 [156254], Figure 5).

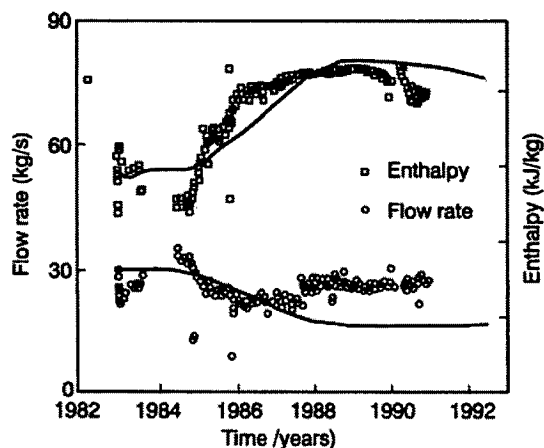
Figure 11.2-3. Typical Variations in Permeability and Porosity in Welded and Unwelded Ash Flow Tuff



NOTE: Water is introduced into the fault in Alcove 8 and collected in and near Niche 3.

Source: Modified from BSC 2002 [157606], Figure 2.

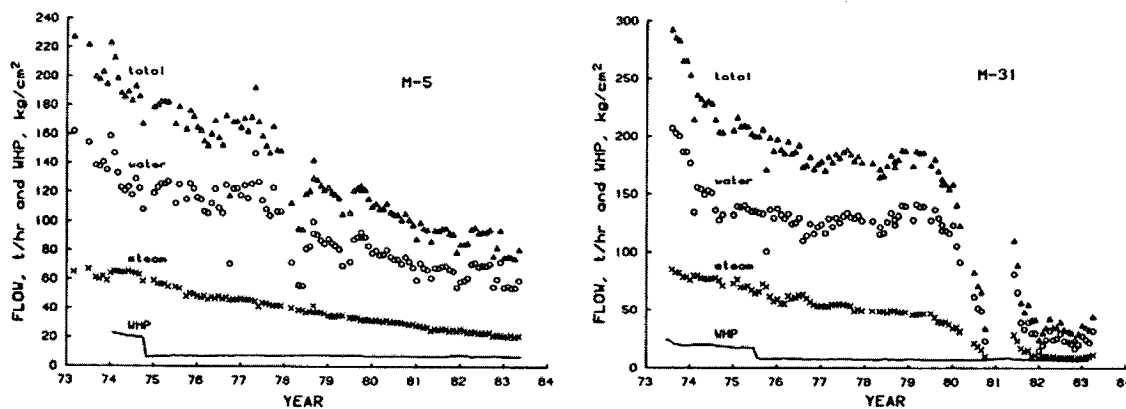
Figure 11.2-4. Schematic Diagram of Flow Test at Yucca Mountain



NOTE: Flow rates are slightly greater and enthalpy is slightly less than predicted by the 1986 model from 1988 to 1992.

Source: Steingrímsson et al. 2000 [156686], p. 2904.

Figure 11.2-5. Comparison between Predicted and Observed Flow Rates and Enthalpies for Well 6 of the Nesjavellir Geothermal Field (Iceland)



NOTE: Well M-31 experienced near-well boiling with abundant mineral deposition. Cleaning well M-31 in 1981 yielded a short-lived increase in production. WHP = well head pressure.

Source: Truesdell et al. 1984 [156350], p. 227.

Figure 11.2-6. Comparison of Production between Wells M-5 and M-31 at the Cerro Prieto Geothermal Field



NOTE: The botryoidal texture of the quartz indicates that it was deposited as chalcidony or amorphous silica, and that this deposition occurred at $>300^{\circ}\text{C}$ due to rapid decompression. qtz = quartz, qtz(chal) = chalcidony, py = pyrite, act = actinolite, and ep = epidote

Source: Moore et al. 2000 [156319], p. 261.

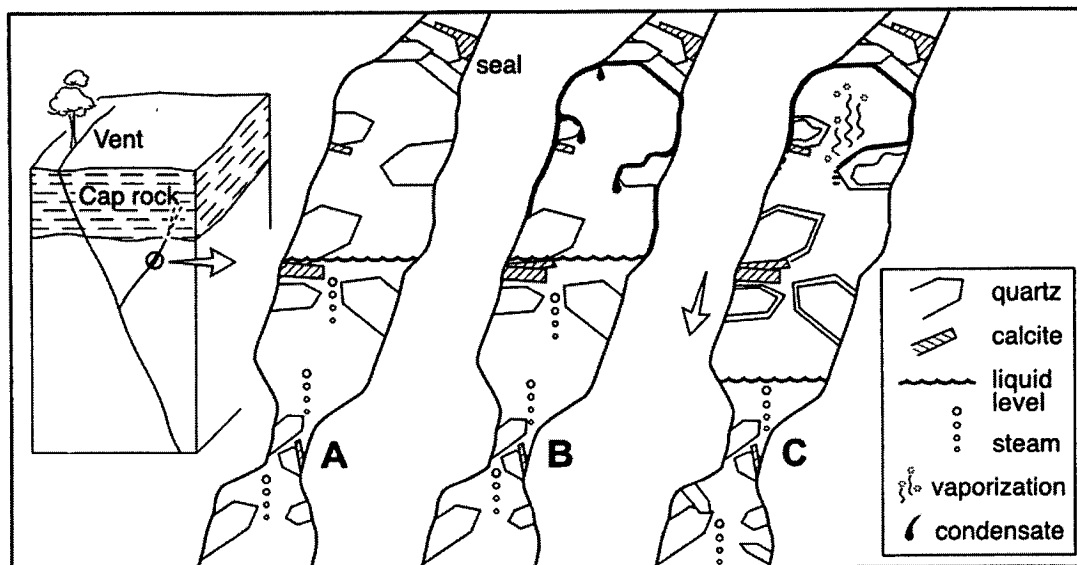
Figure 11.2-7. Photomicrograph of Fracture Minerals in the Karaha-Telaga Bodas System, Indonesia



NOTE: Titanium-rich scale coats anhydrite and fine needles of actinolite. The scale is peeling off the top of the crystal.

Source: Moore et al. 2000 [156319], p. 260.

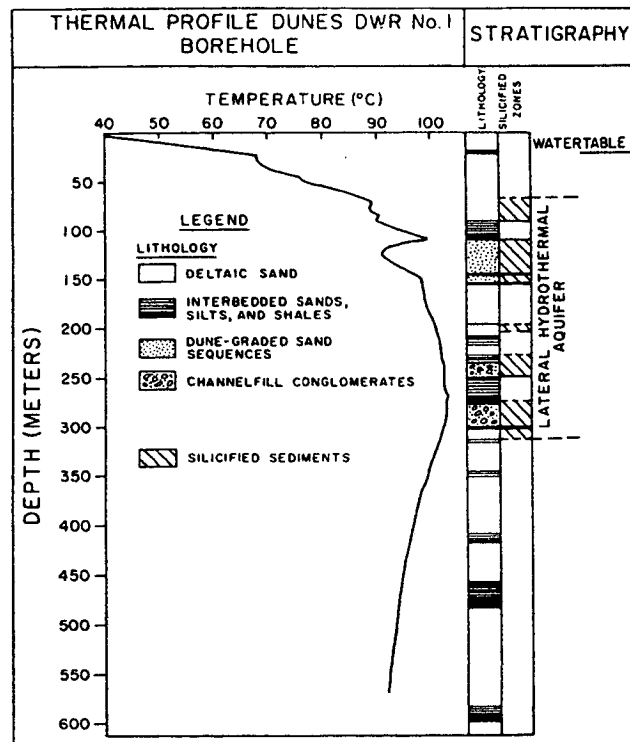
Figure 11.2-8. Scanning Electron Microscope Backscattered Image of Fracture Minerals in the Karaha-Telaga Bodas System, Indonesia



NOTE: In A, quartz and calcite are deposited as the result of boiling possibly due to depressurization in the system. Initially, the rock is too hot for condensation to occur. In B, the top portion of the vein has cooled sufficiently so that condensation occurs. Steam from below migrates through the vein until it reaches the cooler rock where condensation occurs. Corrosion of quartz and calcite occurs near the site of condensation. In C, subsequent lowering of the water table (indicated by the arrow) due to venting results in quartz and calcite deposition due to condensate boiling. Mineral deposition may also occur as condensate reaches the lower, superheated region, and in the liquid-dominated portion of the vein.

Source: Moore et al 2000 [156318], p. 1731.

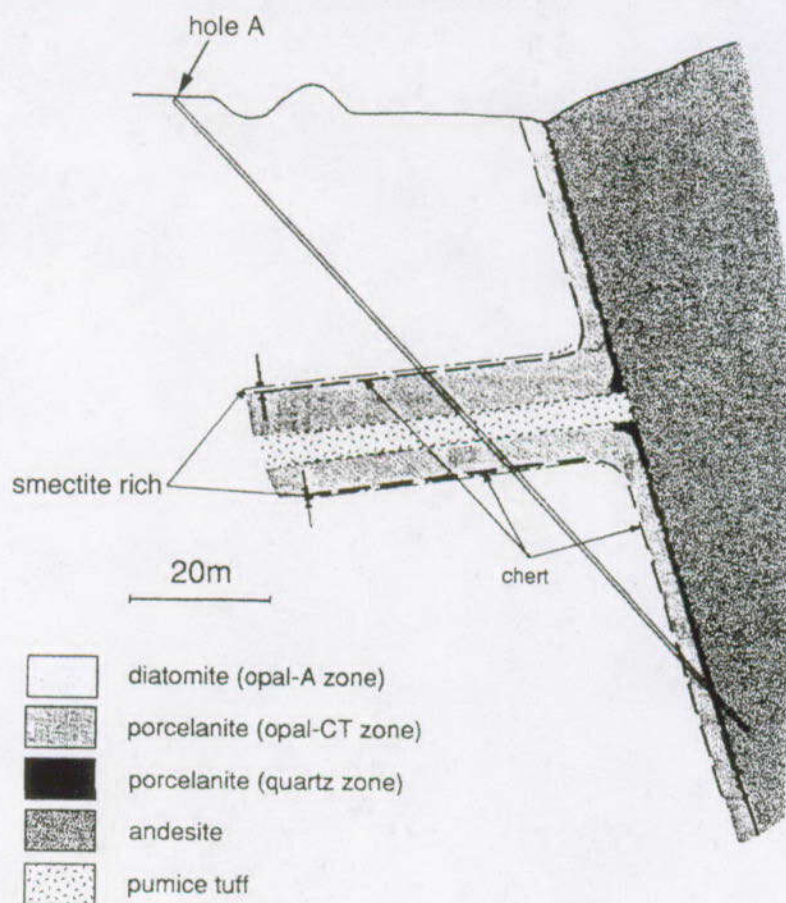
Figure 11.2-9. Schematic Illustration Showing the Transition from a Liquid Dominated System to a Vapor-Dominated System, Showing only a Portion of the Vein



NOTE: The silicified regions are identified in the right column by cross hatching.

Source: Bird and Elders 1976 [154601], p. 286.

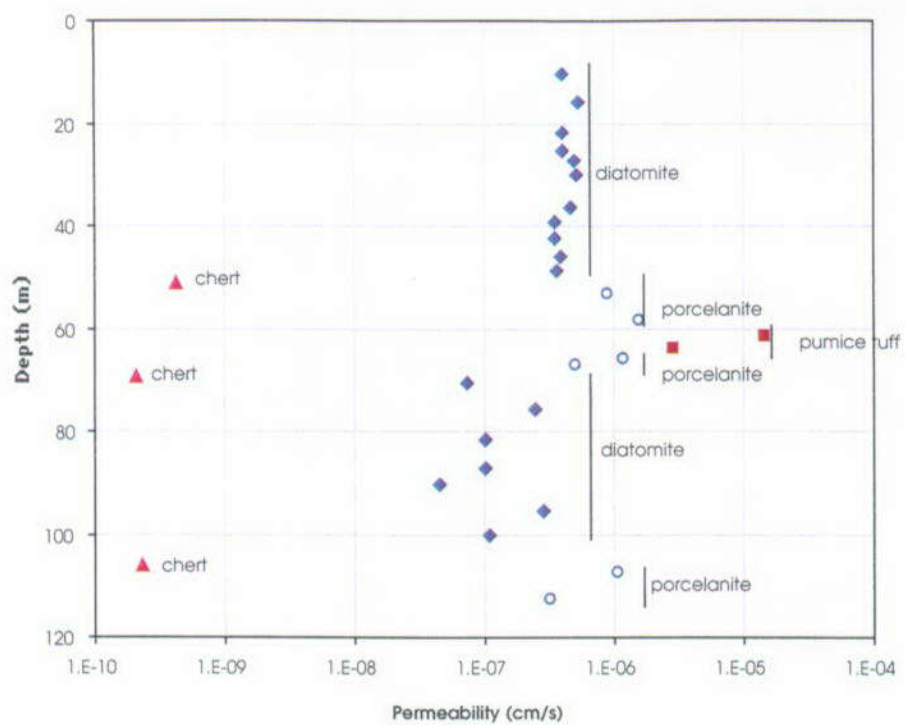
Figure 11.2-10. Temperature Profile and Lithology of Borehole DWR No. 1 at the Dunes Geothermal System, California



NOTE: The diatomite was altered to porcelainite and chert as a result of a hydrothermal system induced by the intrusion of an andesite dike. The thicknesses of the porcelainite and chert layers range from 20 cm to 20 m (porcelainite) and 5 cm to 20 cm (chert).

Source: Chigira and Nakata 1996 [156349], p. 15.

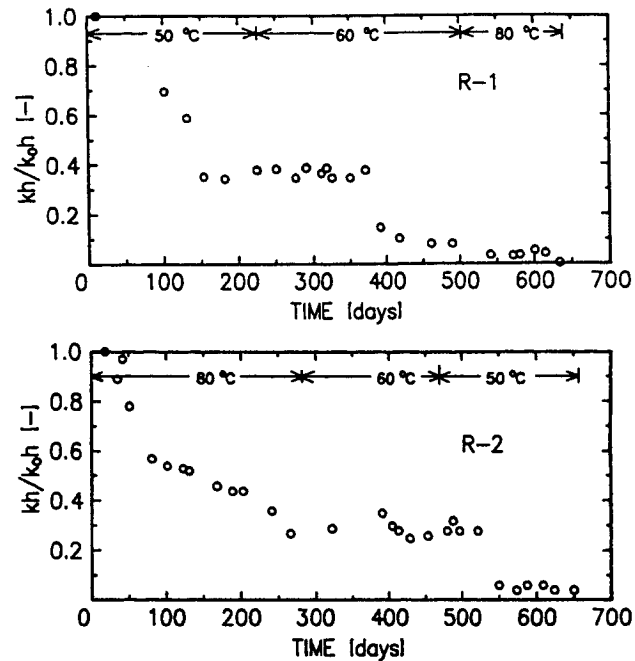
Figure 11.2-11. Schematic of Lithology near Borehole A in the Miocene Iwaya Formation, Japan



NOTE: Alteration mineral porcelainite has a similar permeability to the original diatomite, but the chert is far less permeable.

Source: Data from Chigira and Nakata 1996 [156349], p. 11.

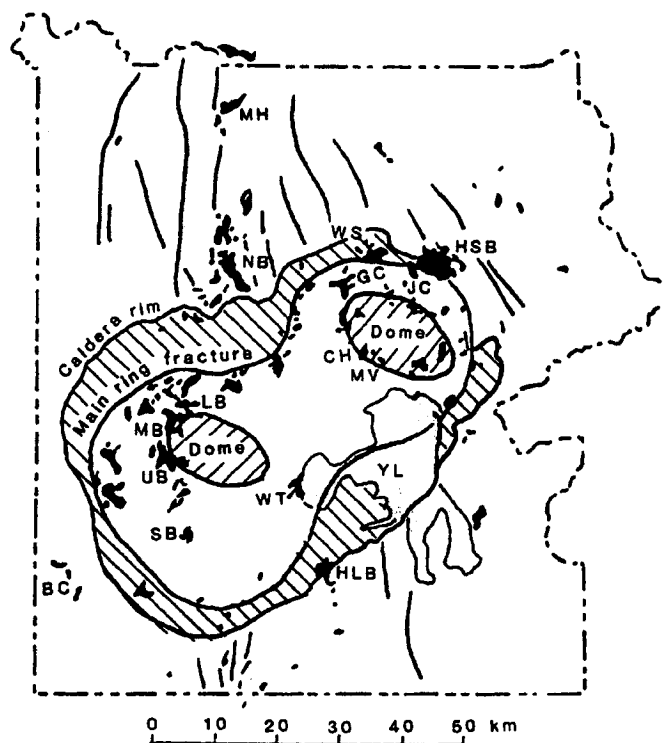
Figure 11.2-12. Permeability Profile of Samples along Borehole A in the Miocene Iwaya Formation, Japan



NOTE: The temperatures indicate the temperature of the injected water. The permeability-thickness product (kh) in Well R-1 decreased from 224 darcy-m to 0.79 darcy-m over 624 days. In Well R-2, the permeability-thickness product decreased from 91 darcy-m to 5 darcy-m over 637 days.
 kh = permeability-thickness product
 k_0h = initial permeability-thickness product

Source: Itoi et al. 1987 [156346], pp. 543-544.

Figure 11.2-13. Reduction in Permeability in Wells R-1 and R-2 over the Duration of a Reinjection Experiment



NOTE: Areas abbreviated as follows: BC = Black Creek, CH = Crater Hills, GC = Grand Canyon, HLB = Hart Lake Basin, HSB = Hot Springs Basin, JC = Joseph's Coat Hot Spring, MH = Mammoth Hot Springs, NB = Norris Geyser Basin, LB = Lower Geyser Basin, MB = Midway Geyser Basin, UB = Upper Geyser Basin, SB = Shoshone Geyser Basin, MV = Mud Volcano, WT = West Thumb, WS = Washburn Hot Springs, YL = Yellowstone Lake.

Source: Fournier 1989 [156245], Figure 2.

Figure 11.3-1. Map of Yellowstone National Park, with Outline of 0.6 Ma Caldera Rim

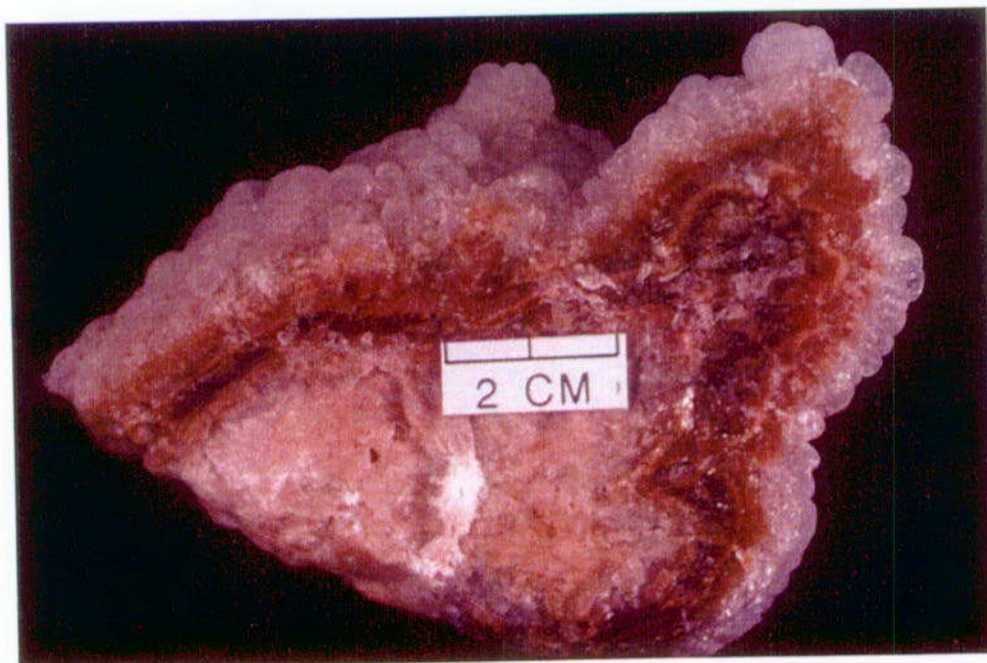


DTN: LB0201YSANALOG.001 [157569]

NOTE: Large sinter blocks had been ejected by 1989 explosion. The pool has an opalescent color, indicating presence of colloidal silica (photo by R. Fournier, USGS).

Source: Simmons 2002 [157578], SN-LBNL-SCI-185-V1, p. 7-1.

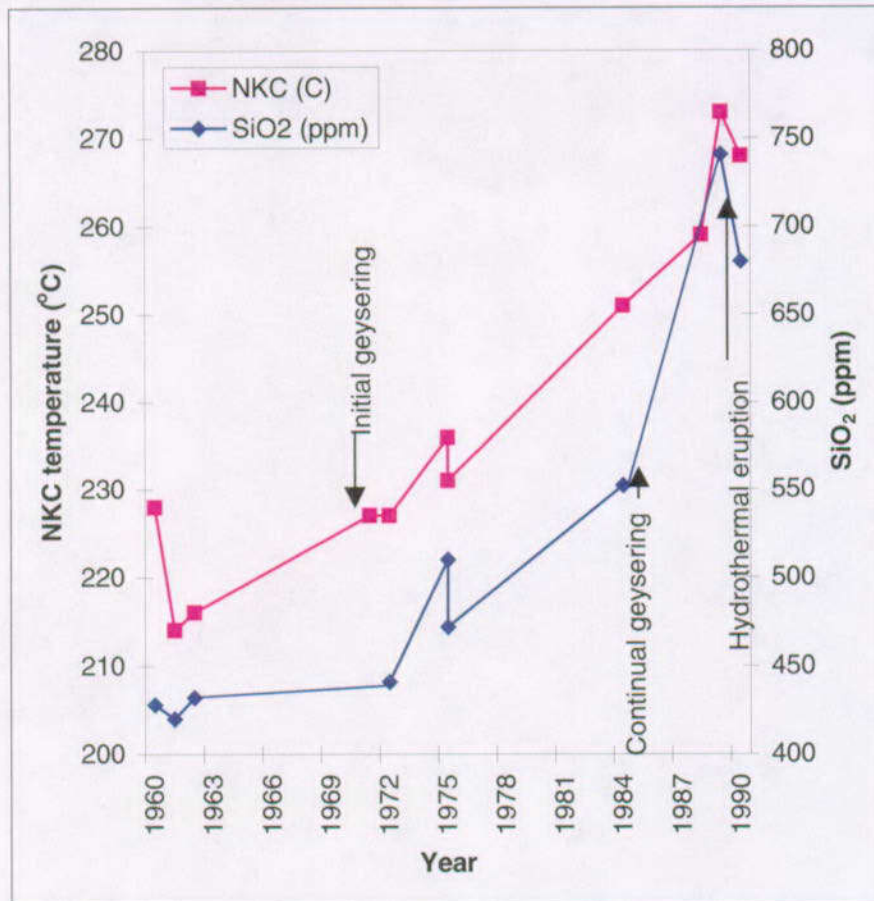
Figure 11.3-2. Porkchop Geyser (July 1991)



DTN: LB0201YSANALOG.001 [157569]

Source: Simmons 2002 [157578], SN-LBNL-SCI-185-V1, p. 7-1.

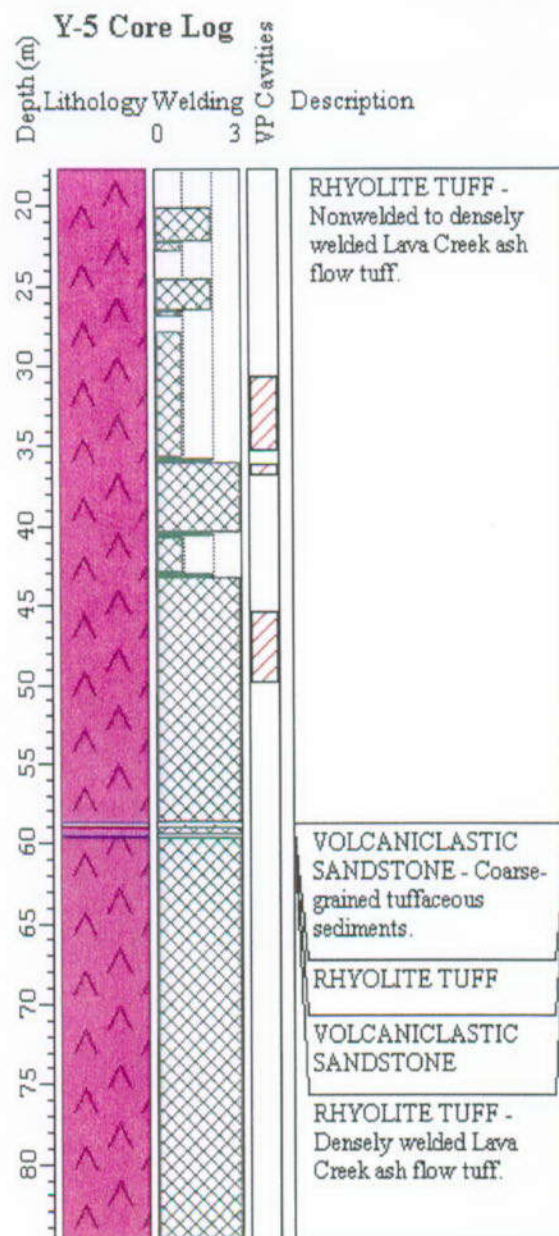
Figure 11.3-3. Block from 1989 Porkchop Geyser Eruption, with Gelatinous, Botryoidal Silica Coating Outer Margins and Cavities (photo from T.E.C. Keith, USGS)



NOTE: Change in flow behavior interpreted to be linked to precipitation of amorphous silica, resulting in the clogging of flow channels.

Source: Fournier et al. 1991 [156246], p. 1116.

Figure 11.3-4. Changes in Calculated Sodium-Potassium-Calcium (NKC) Reservoir Temperatures and Silica Concentrations for Waters Sampled from Porkchop Geyser

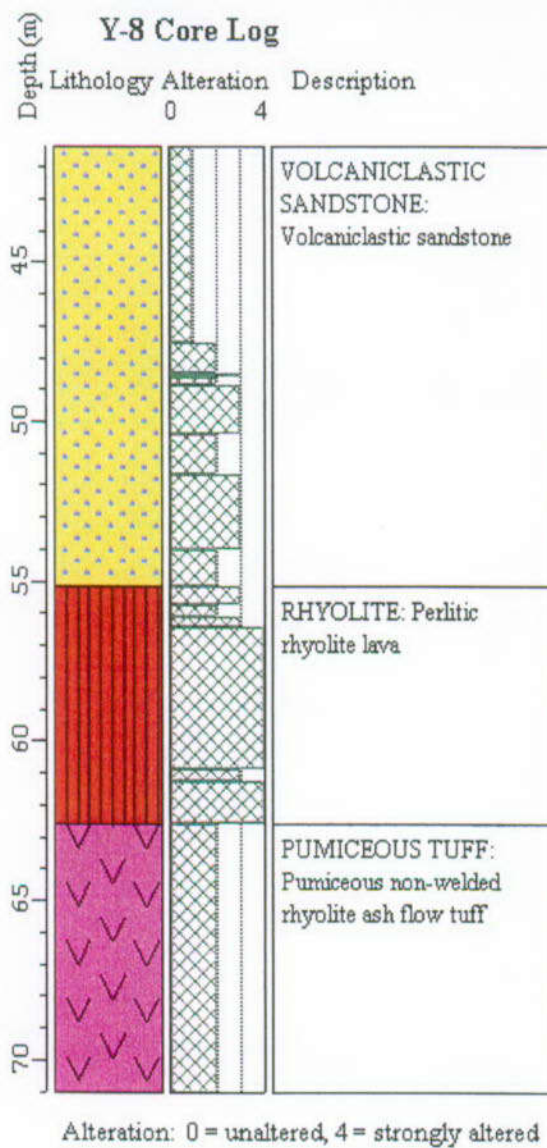


Degree of welding: 0 = nonwelded, 1 = weakly welded, 2 = moderately welded, 3 = densely welded.
VP = vapor-phase

DTN: LB0201YSANALOG.001 [157569]

Source: Dobson et al. 2001 [154547], Figure 2.

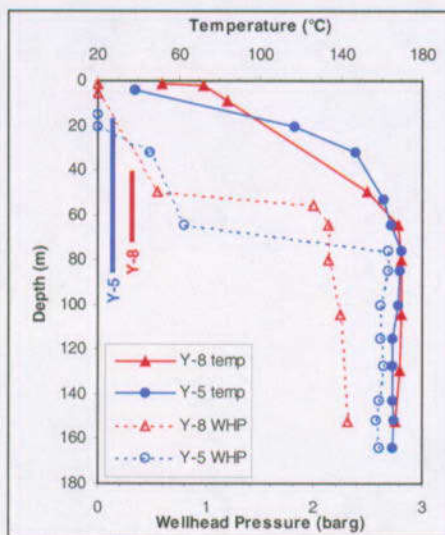
Figure 11.3-5. Simplified Geologic Log of the Y-5 Core



DTN: LB0201YSANALOG.001 [157569]

Source: Dobson et al. 2001 [154547], Figure 3.

Figure 11.3-6. Simplified Geologic Log of the Y-8 Core

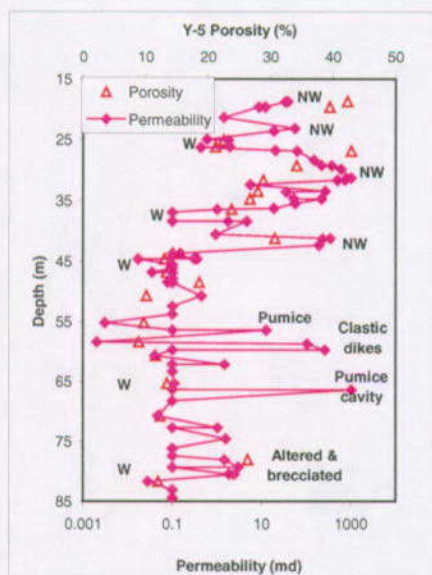


DTN: LB0201YSANALOG.001 [157569]

NOTE: Vertical bars at left indicate studied core-depth intervals. Temperature and pressure data from White et al. 1975 [154530].

Source: Dobson et al. 2001 [154547], Figure 1.

Figure 11.3-7. Downhole Temperature (Solid Lines) and Wellhead Pressure Variations (Dotted Lines) in the Y-5 and Y-8 Wells

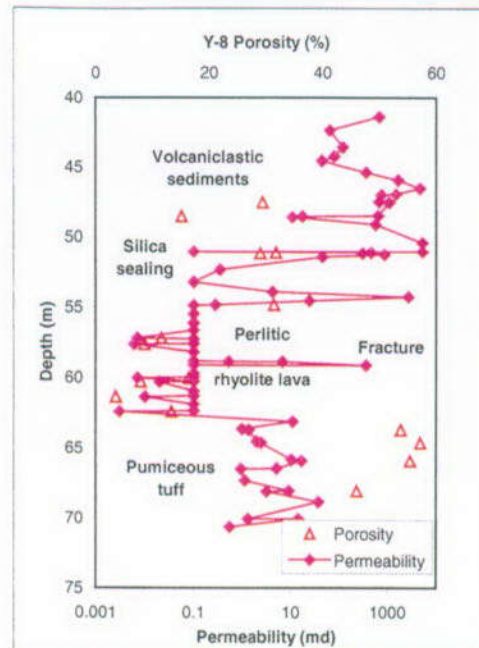


DTN: LB0201YSANALOG.001 [157569]

NOTE: W= moderately to densely welded tuff, NW = nonwelded to weakly welded tuff. The 0.1 md values represent the lower detection limit for minipermeability measurements; actual values are lower.

Source: Dobson et al. 2001 [154547], Figure 4.

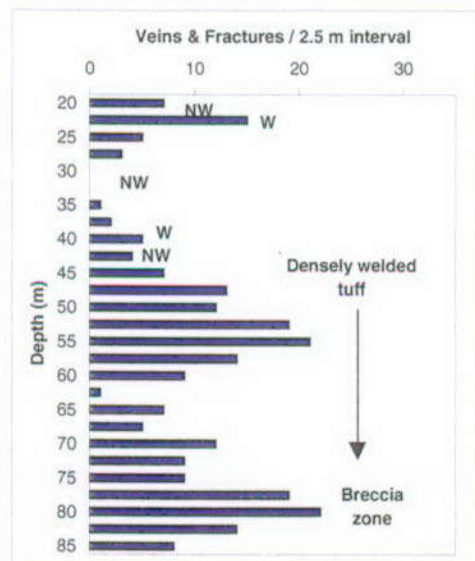
Figure 11.3-8. Porosity and Permeability Variations in the Y-5 core



DTN: LB0201YSANALOG.001 [157569]

Source: Dobson et al. 2001 [154547], Figure 5.

Figure 11.3-9. Porosity and Permeability Variations in the Y-8 Core

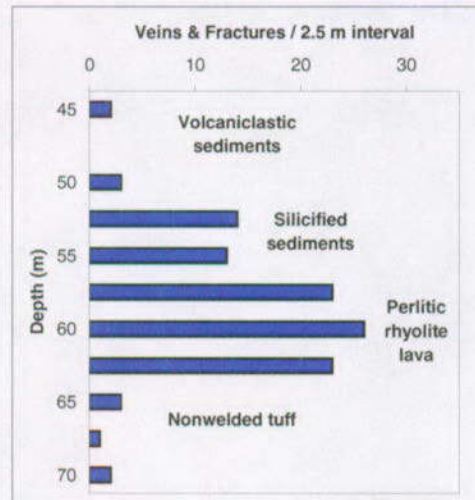


DTN: LB0201YSANALOG.001 [157569]

NOTE: W= moderately to densely welded tuff, NW = nonwelded to weakly welded tuff

Source: Dobson et al. 2001 [154547], Figure 6.

Figure 11.3-10. Veins and Fractures in the Y-5 Core



DTN: LB0201YSANALOG.001 [157569]

Source: Dobson et al. 2001 [154547], Figure 8.

Figure 11.3-11. Veins and Fractures in the Y-8 Core

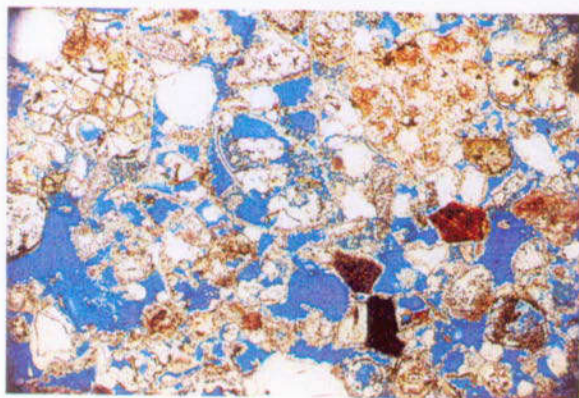


DTN: LB0201YSANALOG.001 [157569]

NOTE: Core width is 4.4 cm. Permeability values of welded tuff clast (A) and matrix (B) are both below the minipermeameter detection limit (0.1 md).

Source: Dobson et al. 2001 [154547], Figure 7.

Figure 11.3-12. Hydrothermal Breccia from the Y-5 Core at 47.7 m (156.5 feet)

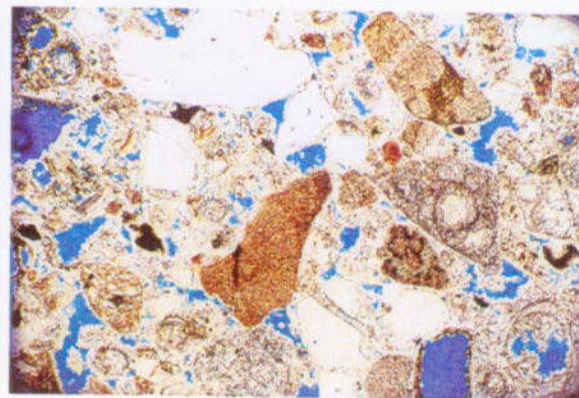


Y-8, 155.9'

1 mm

Permeability = 1030 md

Porosity = 29.2%



Y-8, 159.2'

1 mm

Permeability = 16.9 md

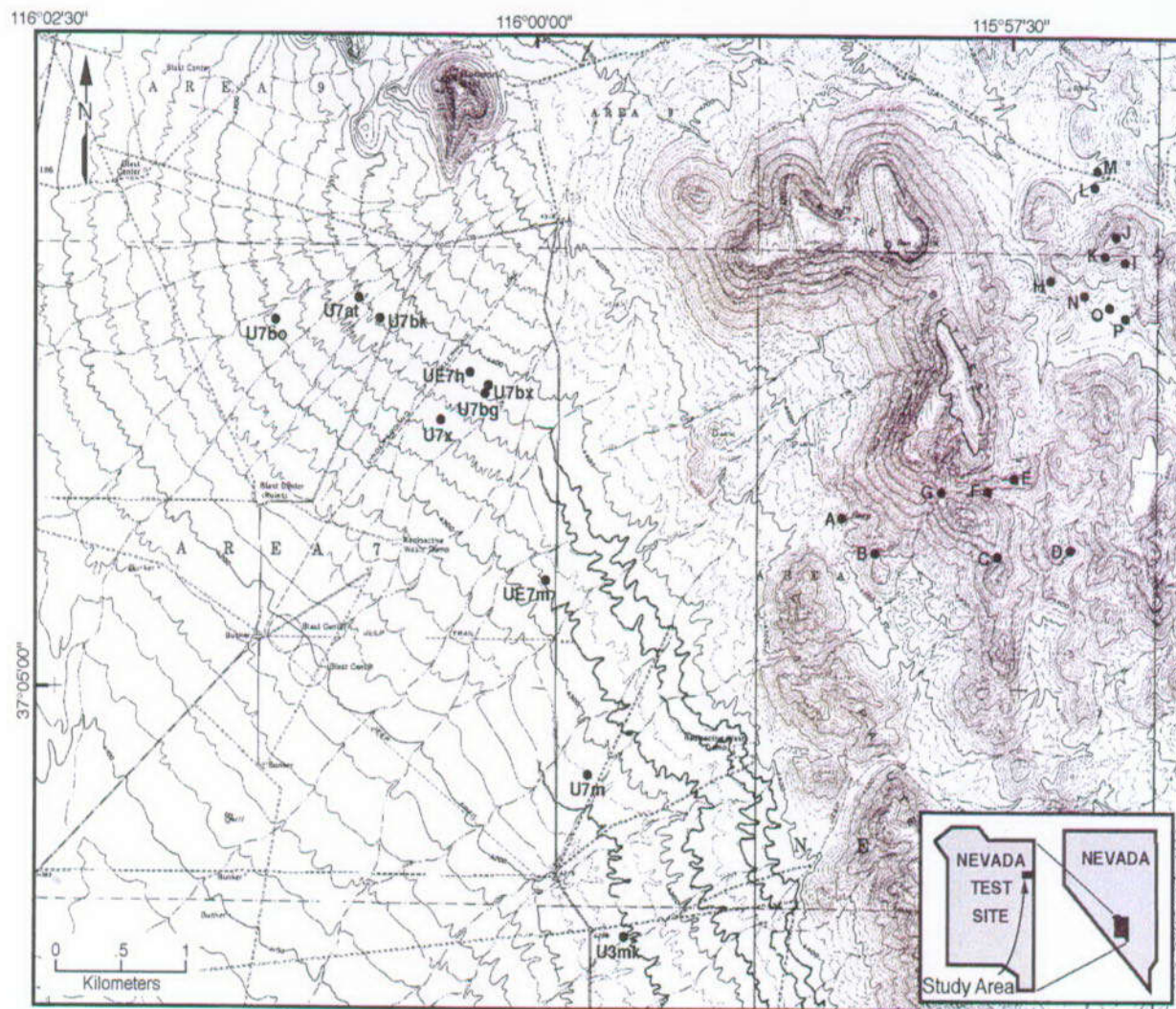
Porosity = 15.0%

DTN: LB0201YSANALOG.001 [157569]

NOTE: Silicification of the sample from 159.2' has resulted in a 50% reduction in porosity (change in abundance of blue epoxy denoting porosity) and decrease in permeability of nearly two orders of magnitude.

Source: Simmons 2002 [157578], SN-LBNL-SCI-185-V1, Roll 17, Photos 2 and 4.

Figure 11.3-13. Photomicrographs of Volcaniclastic Sandstone Unit from Y-8 Core



NOTE: Sampling sections, labeled with single letters, and drill holes, which all start with U, are indicated on the right and left sides of the figure, respectively. The stratigraphic units of the drill holes are given in Table 11.4-2.

Source: Simmons 2002 [157578] SN-LANL-SCI-215-V1, p. 6.

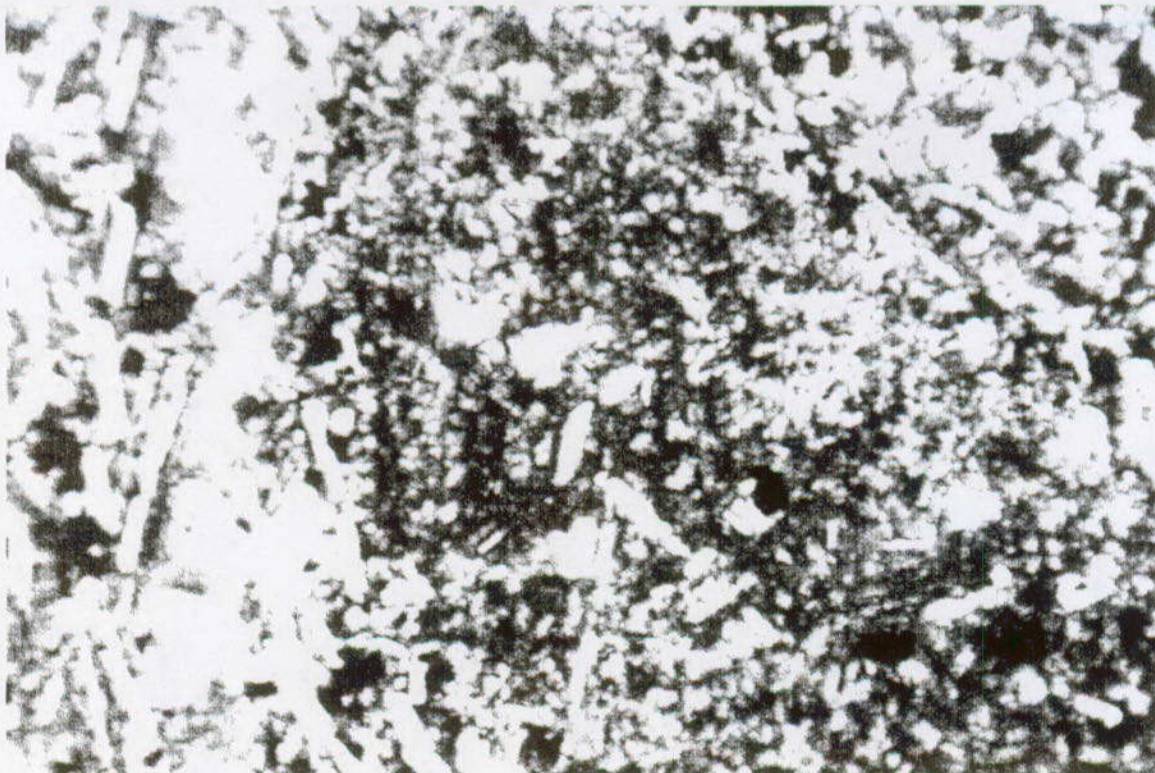
Figure 11.4-1. Location Map of the Paiute Ridge Basaltic Intrusion Complex in the Nevada Test Site



NOTE: These veins are within 8 ft (2.4 m) from the basaltic intrusion contact adjacent to the Papoose Lake Sill in the northern part of Paiute Ridge. The vein zone is about 25 ft (7.6 m) wide.

Source: Simmons 2002 [157578]; SN-LANL-SCI-215-V1, p.44, Figure 16B.

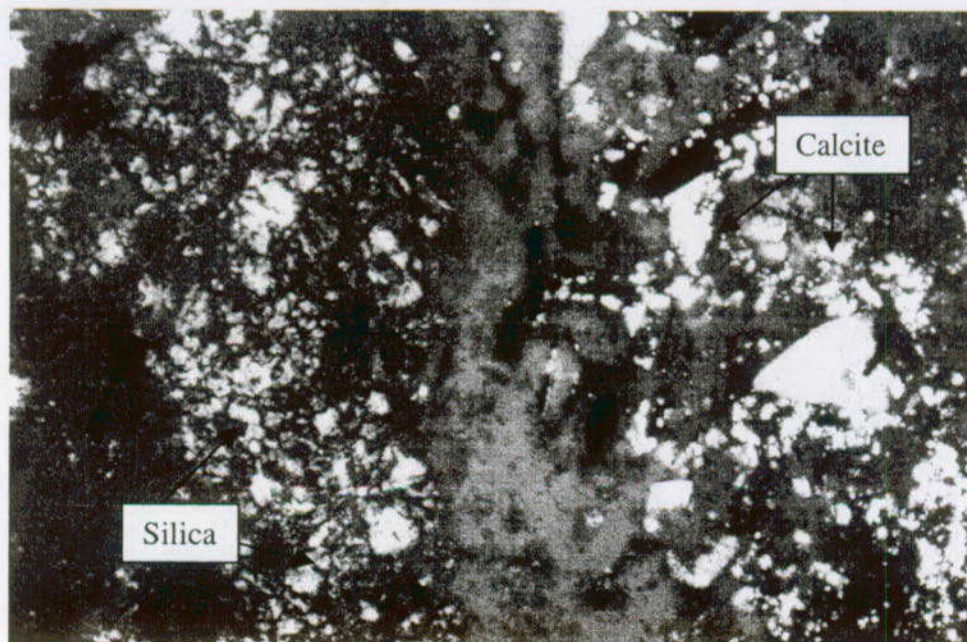
Figure 11.4-2. Anastomosing Opal Veins Adjacent to Papoose Lake Sill



NOTE: Calcite veins along fractures and cavities and epidote grains in cavities are present in the photomicrograph of basalt (LANL# 3547) (view is 170 x 255 μm).

Source: Simmons 2002 [157578], SN-LANL-SCI-215-V1, p. 130.

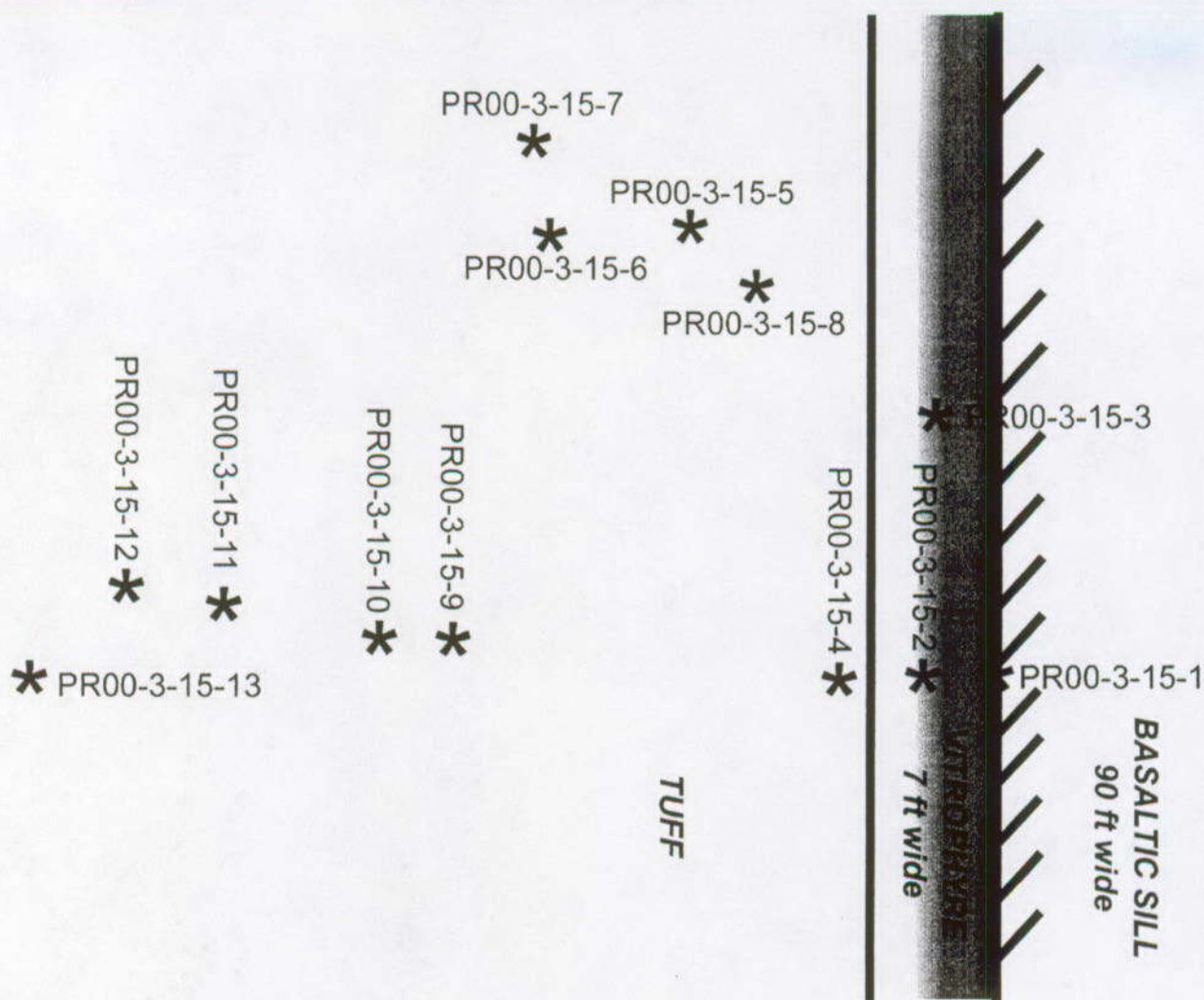
Figure 11.4-3. Photomicrograph of Basalt from the Contact Zone of the Papoose Lake Sill in the Northern Part of Paiute Ridge



NOTE: This sample (LANL# 3557) was collected 43 ft (13.1 m) from the Papoose Lake Sill contact. Brighter patches of silica (left) and calcite (right) separated by opaque material replace the vitric matrix (view is 70 x 110 μm).

Source: Simmons 2002 [157578]; SN-LANL-SCI-215-V1, p. 131.

Figure 11.4-4. Photomicrograph of Altered Rainier Mesa Tuff



NOTE: Map not to scale; compiled from field notes; see Table 11.4-1 for sample descriptions and measured distances from sill margin.

Source: Simmons 2002 [157578], SN-LBNL-SCI-108-V2, p. 23.

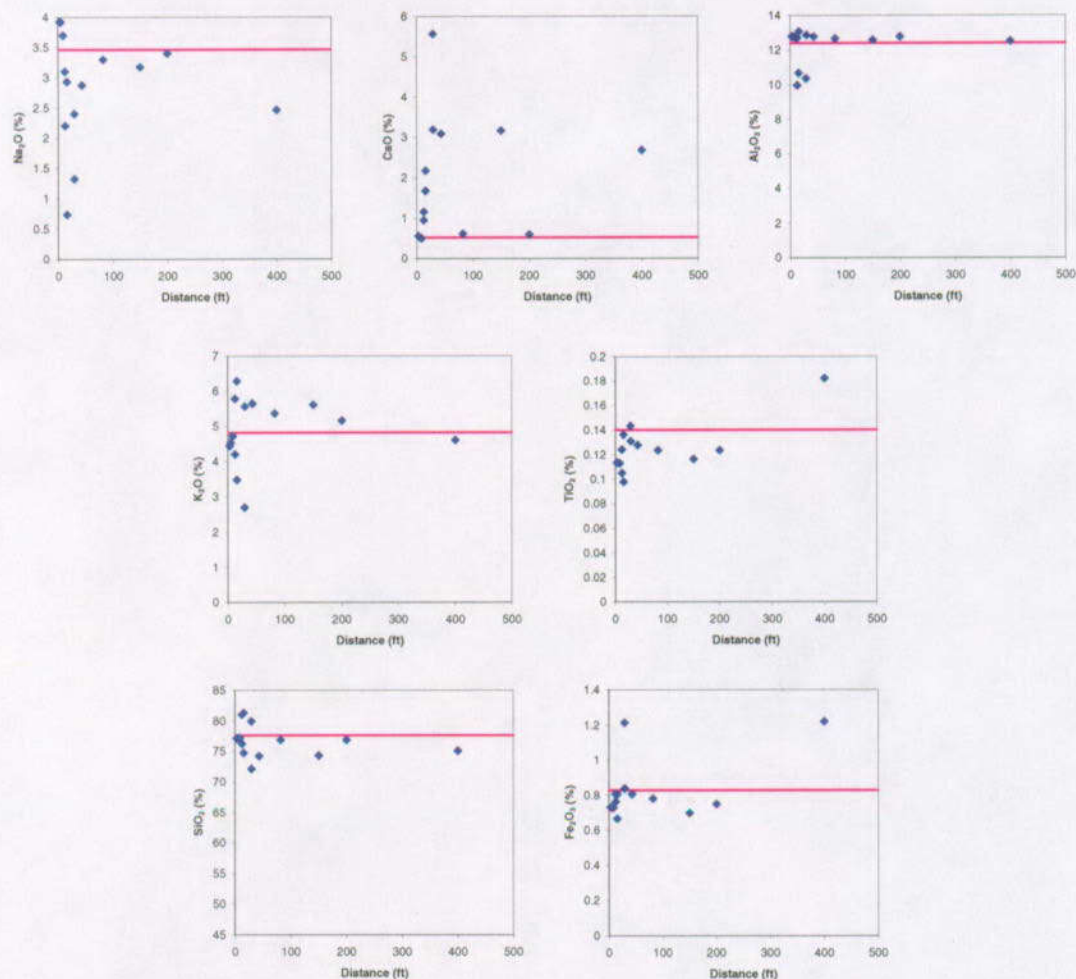
Figure 11.4-5. Schematic Map of Location H, Papoose Lake Basaltic Sill, Paiute Ridge, Nevada Test Site



NOTE: This sample of nonwelded Rainier Mesa Tuff (LANL# 3559) was collected 200 ft (61 m) from the basaltic sill contact. It is apparent that the vesicles are devoid of secondary minerals from devitrification after deposition or from the hydrothermal process related to the basaltic intrusion.

Source: Simmons 2002 [157578]; SN-LANL-SCI-215-V1, p. 101.

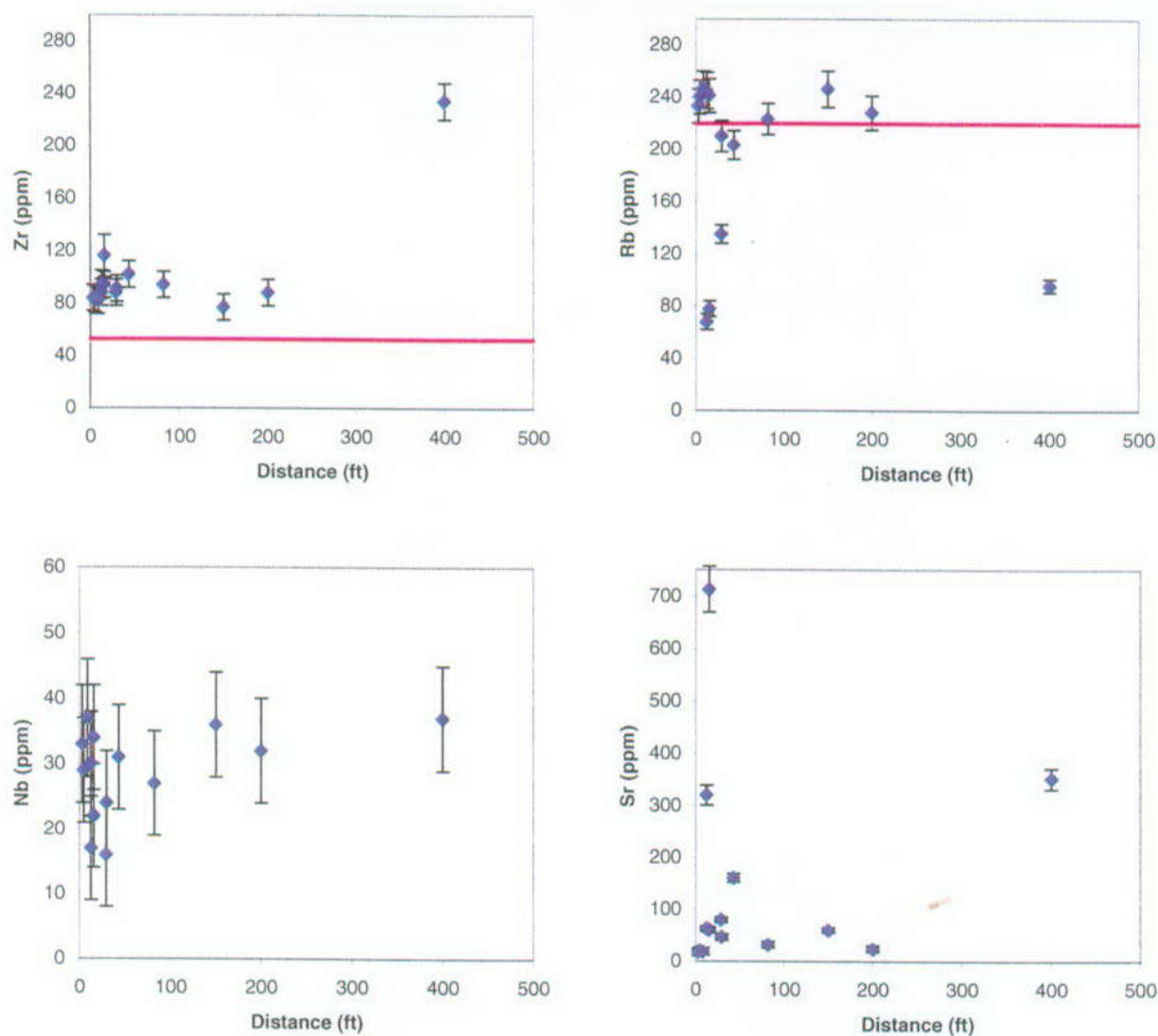
Figure 11.4-6. Scanning Electron Microscope Image of Vesicles in Nonwelded Rainier Mesa Tuff



NOTE: These variation diagrams use data in feet for distance and wt% for Na₂O, K₂O, Al₂O₃, CaO, SiO₂, TiO₂, and Fe₂O₃ of tuff samples from the northern part of Paiute Ridge. Major-element contents are calculated to 100% volatile free. Total iron reported as Fe₂O₃. Line indicates average composition of Rainier Mesa rhyolitic tuff reported by Broxton et al. (1989 [100024], Table 3).

Source: Simmons 2002 [157578]; SN-LANL-SCI-215-V1, pp. 63, 69–76.

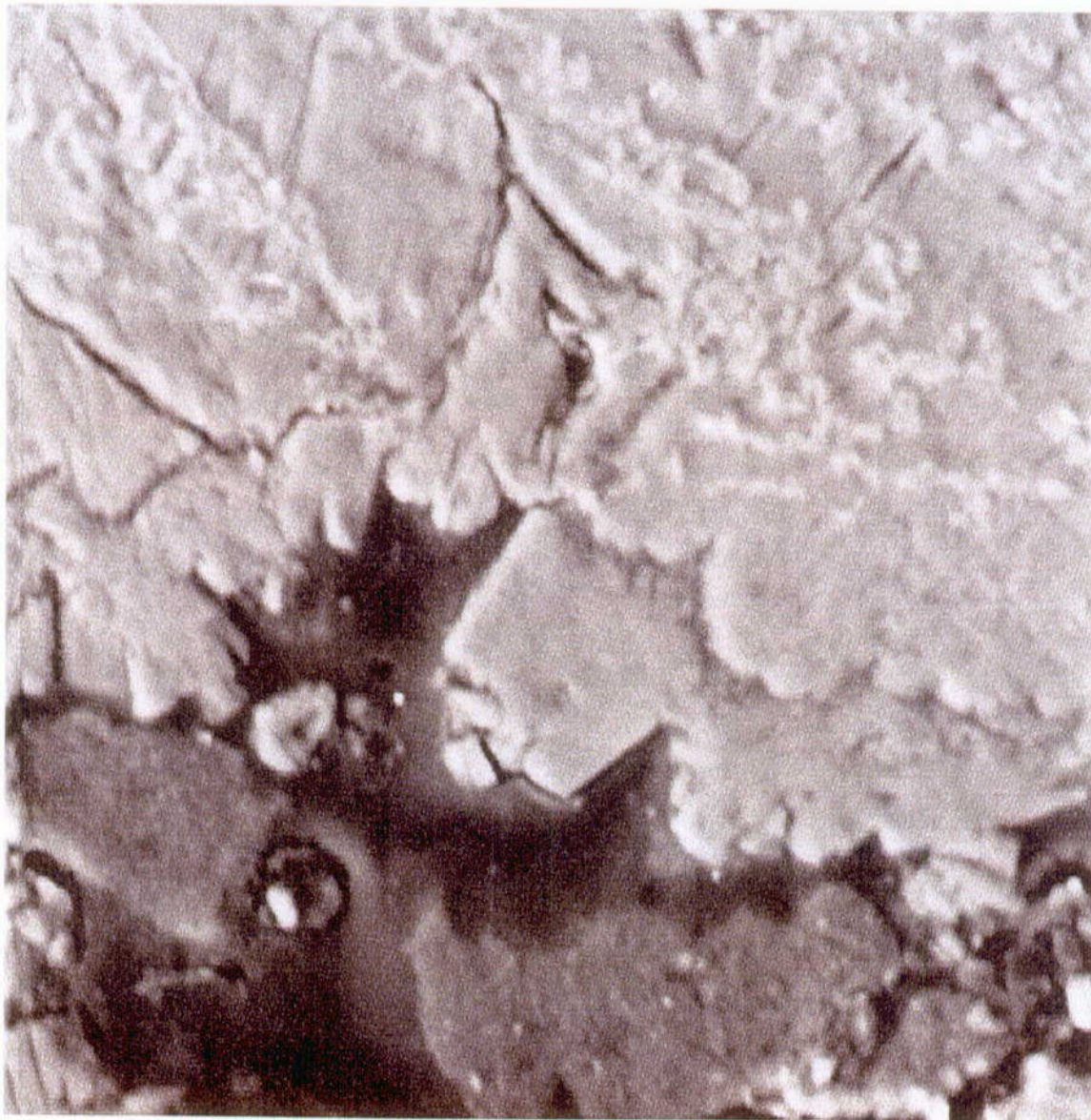
Figure 11.4-7. Variation Diagrams of Distance Versus Na₂O, K₂O, Al₂O₃, CaO, SiO₂, TiO₂, and Fe₂O₃



NOTE: These variation diagrams use data in feet for distance versus ppm for Zr, Rb, Nb, and Sr of tuff samples from the northern part of Paiute Ridge. Line indicates average composition of Rainier Mesa rhyolitic tuff reported by Broxton et al. (1989 [100024], Table 3).

Source: Simmons 2002 [157578]; SN-LANL-SCI-215-V1, pp. 63, 69–76.

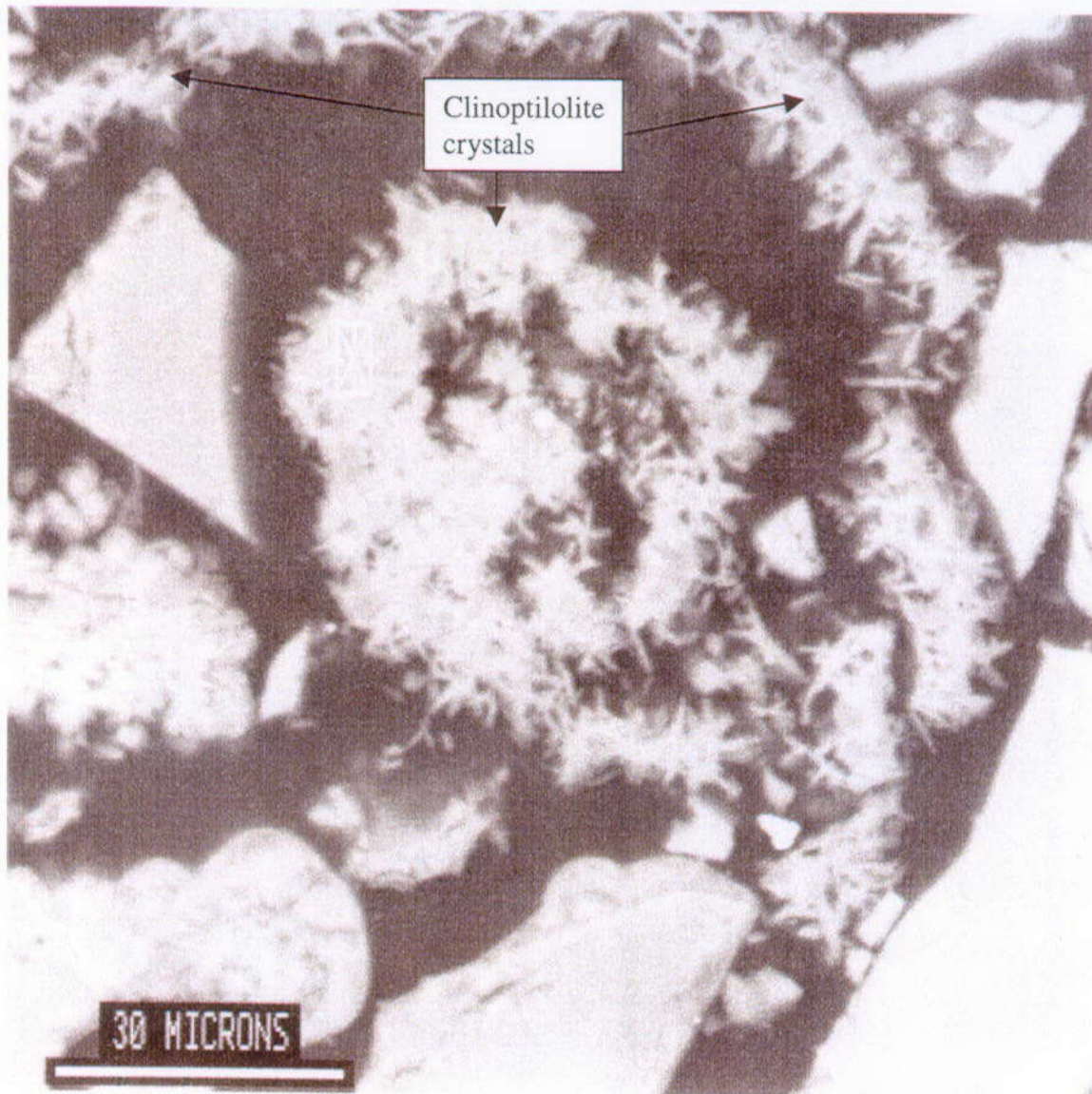
Figure 11.4-8. Variation Diagrams of Distance Versus Zr, Rb, Nb, and Sr



NOTE: 500 μm scale

Source: Simmons 2002 [157578]; SN-LANL-SCI-215-V1, p. 128.

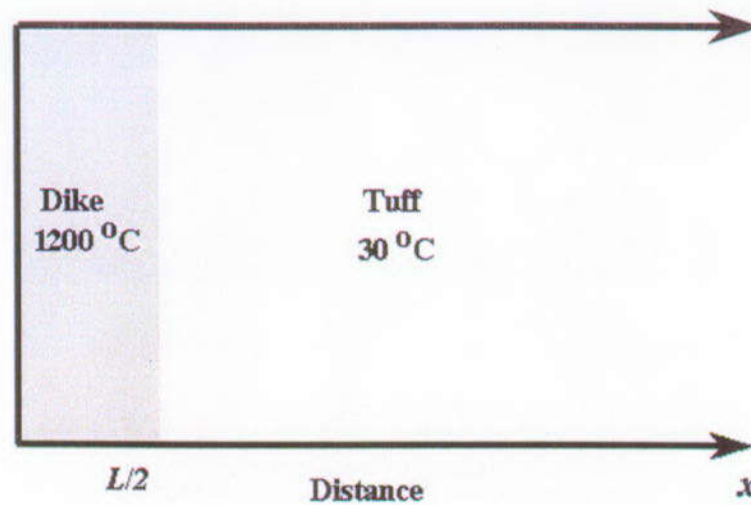
Figure 11.4-9a. Tabular Crystal of Clinoptilolite Overgrowth on a Second Layer of Clinoptilolite with Scalloped or Serrated Edges (LANL# 3552)



NOTE: This sample of Rainier Mesa Tuff (LANL# 3550) was collected 8.5 ft (2.6 m) from the Papoose Lake Sill contact in the northern part of Paiute Ridge. It is apparent that the cavity is partially filled by clinoptilolite.

Source: Simmons 2002 [157578]; SN-LANL-SCI-215-V1, p. 100.

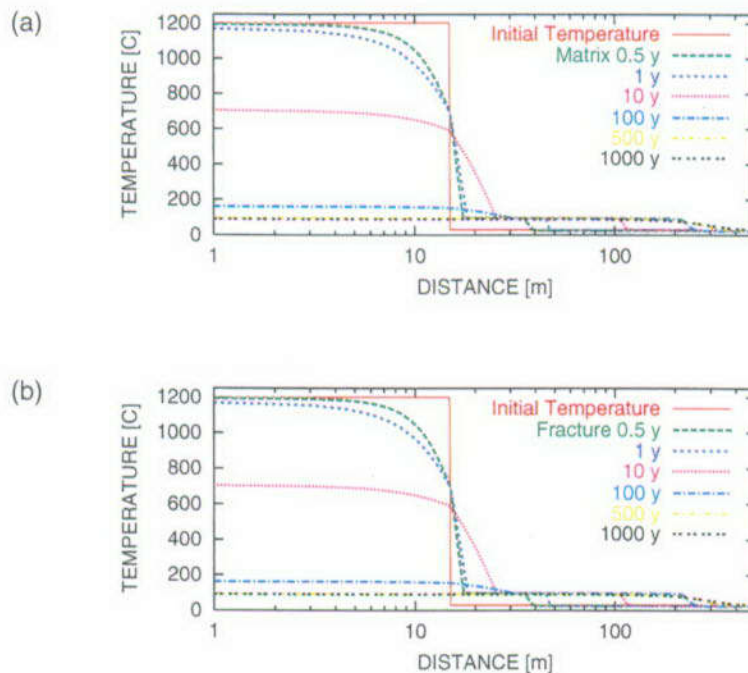
Figure 11.4-9b. Scanning Electron Microscope Image of Clinoptilolite Crystal Aggregates in a Cavity of Rainier Mesa Tuff



NOTE: This diagram of the half-space computational domain indicates the initial temperature of the intrusion of thickness L and tuff country rock for a one-dimensional simulation perpendicular to the intrusion.

Source: Simmons 2002 [157578], SN-LBNL-SCI-108-V2, p. 22.

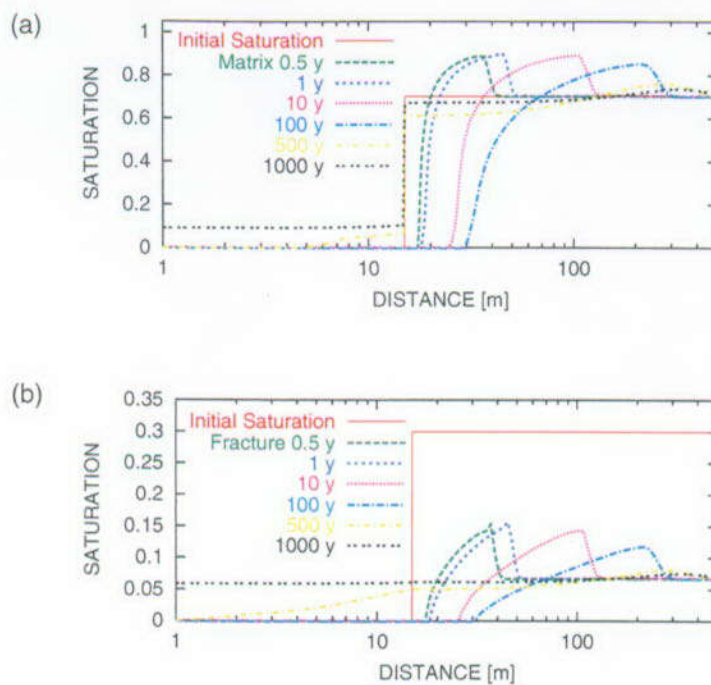
Figure 11.4-10. Schematic Diagram of the Half-space Computational Domain



NOTE: $\sigma_{fm} = 10^2$

Source: Simmons 2002 [157578]; SN-LANL-SCI-215-V1, p. 112.

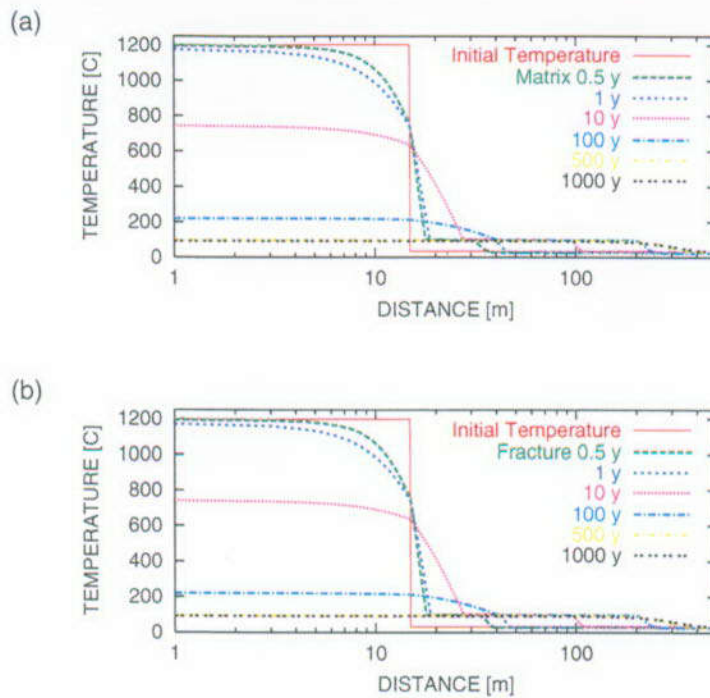
Figure 11.4-11. Matrix (a) and Fracture (b) Temperature Profiles as a Function of Distance at the Indicated Times for the Dual-Continuum Model with Strong Fracture-Matrix Coupling



NOTE: $\sigma_{fm} = 10^2$

Source: Simmons 2002 [157578]; SN-LANL-SCI-215-V1, p. 112.

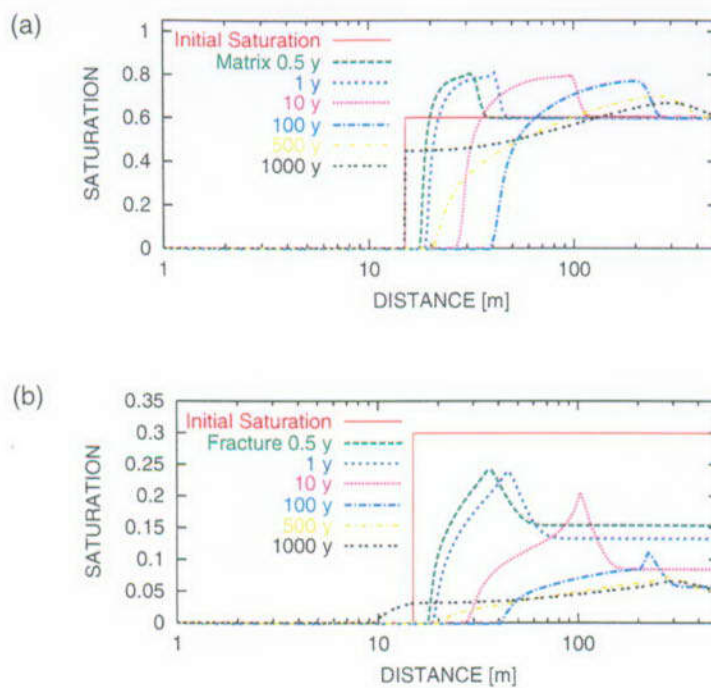
Figure 11.4-12. Matrix (a) and Fracture (b) Saturation Profiles as a Function of Distance at the Indicated Times for the Dual-Continuum Model with Strong Fracture-Matrix Coupling



NOTE: $\sigma_{fm} = 10^{-2}$

Source: Simmons 2002 [157578]; SN-LANL-SCI-215-V1, p. 111.

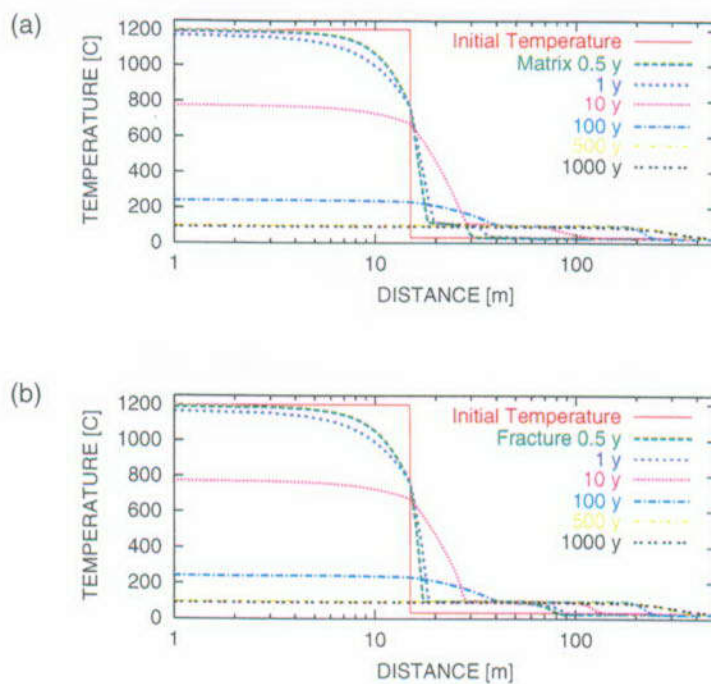
Figure 11.4-13. Matrix (a) and Fracture (b) Temperature Profiles as a Function of Distance at the Indicated Times for the Dual-Continuum Model with Moderate Fracture-Matrix Coupling



NOTE: $\sigma_{fm} = 10^{-2}$

Source: Simmons 2002 [157578]; SN-LANL-SCI-215-V1, p. 111.

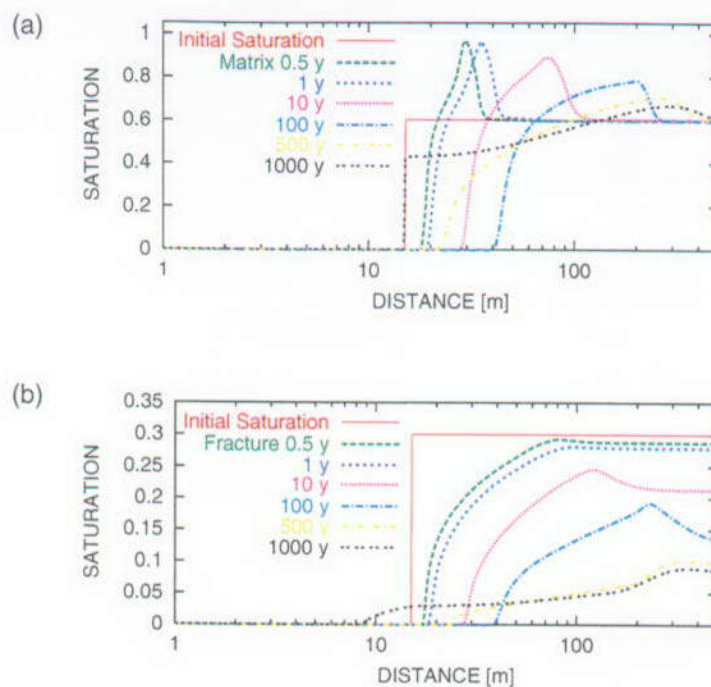
Figure 11.4-14. Matrix (a) and Fracture (b) Saturation Profiles as a Function of Distance at the Indicated Times for the Dual-Continuum Model with Moderate Fracture-Matrix Coupling



NOTE: $\sigma_{fm} = 10^{-4}$

Source: Simmons 2002 [157578]; SN-LANL-SCI-215-V1, p. 110.

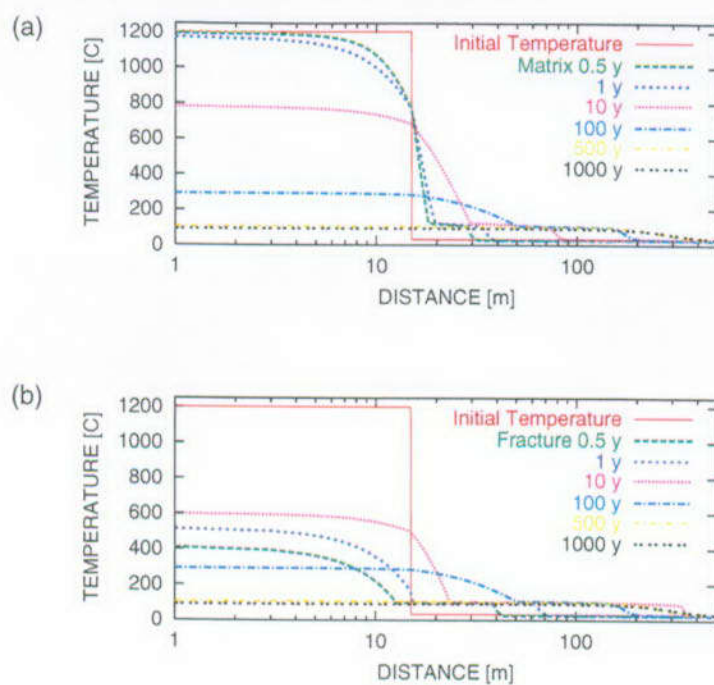
Figure 11.4-15. Matrix (a) and Fracture (b) Temperature Profiles as a Function of Distance at the Indicated Times for the Dual-Continuum Model with Weak Fracture-Matrix Coupling



NOTE: $\sigma_{lm} = 10^{-4}$

Source: Simmons 2002 [157578]; SN-LANL-SCI-215-V1, p. 110.

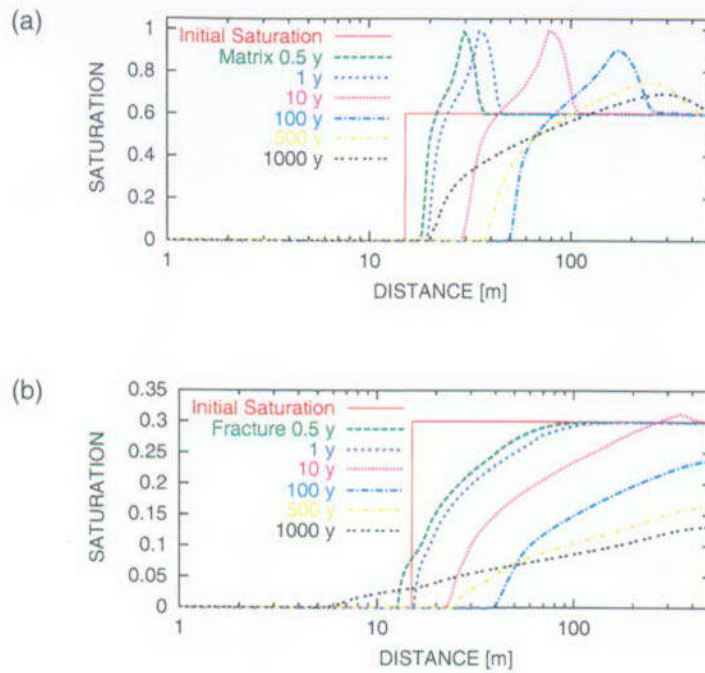
Figure 11.4-16. Matrix (a) and Fracture (b) Saturation Profiles as a Function of Distance at the Indicated Times for the Dual-Continuum Model with Weak Fracture-Matrix Coupling



NOTE: $\sigma_{fm} = 10^{-6}$

Source: Simmons 2002 [157578]; SN-LANL-SCI-215-V1, p. 107.

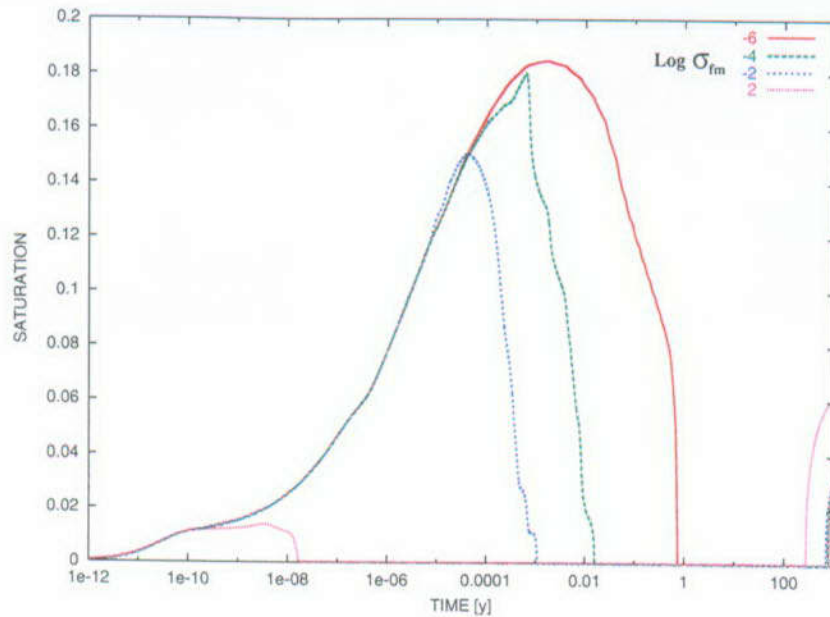
Figure 11.4-17. Matrix (a) and Fracture (b) Temperature Profiles as a Function of Distance at the Indicated Times for the Dual-Continuum Model with Very Weak Fracture-Matrix Coupling



NOTE: $\sigma_{fm} = 10^{-6}$

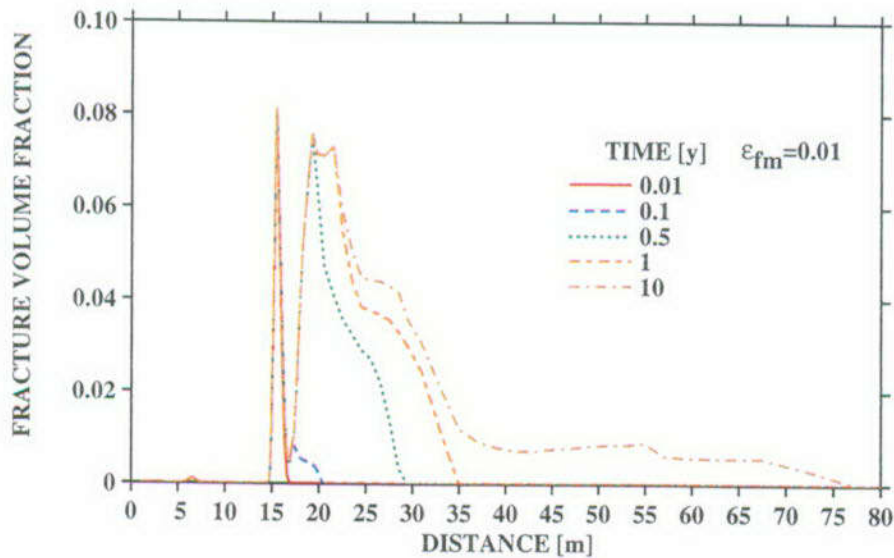
Source: Simmons 2002 [157578]; SN-LANL-SCI-215-V1, p. 107.

Figure 11.4-18. Matrix (a) and Fracture (b) Saturation Profiles as a Function of Distance at the Indicated Times for the Dual-Continuum Model with Very Weak Fracture-Matrix Coupling



Source: Simmons 2002 [157578]; SN-LANL-SCI-215-V1, p. 118.

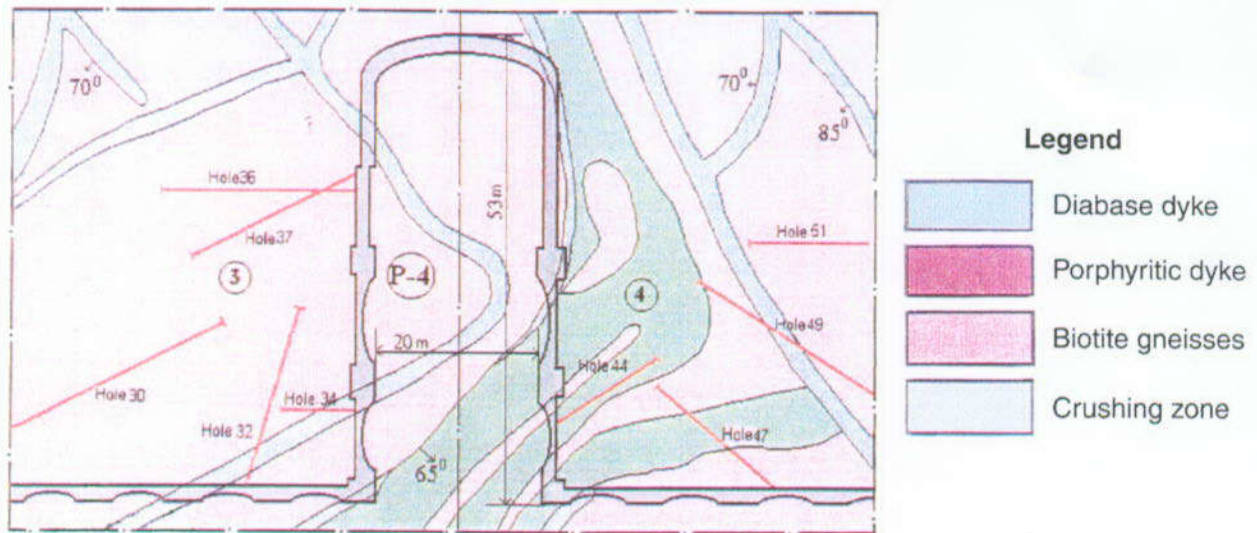
Figure 11.4-19. Fracture Saturation as a Function of Time at the Boundary between the Intrusion and Country Rock for Different Fracture-Matrix Coupling Strengths



NOTE: $\sigma_{fm} = 10^{-2}$

Source: Simmons 2002 [157578]; SN-LANL-SCI-215-V1, p. 117.

Figure 11.4-20. Fracture Volume Fraction of Amorphous Silica Precipitation as a Function of Distance for Various Times with Moderate Fracture-Matrix Coupling



Source: Gupalo et al. 1999 [157470], Figure 2.16.

Figure 11.6-1. Schematic of the Underground Workings at Facility P-4 at K-26, Siberia, in Cross Section

Table 11.2-1. THC Processes in Geothermal Systems and Their Applicability to Yucca Mountain

THC process	Geothermal system component	Geothermal examples	Applicability to Yucca Mountain	Potential impact to repository performance
Advective heating	Heat transfer within convecting geothermal reservoir: develop near-isothermal vertical thermal profiles	Nearly ubiquitous: examples include Yellowstone (Wyoming), Salton Sea (California), Wairakei (New Zealand)	Would only occur very locally in high-temperature ($>100^{\circ}\text{C}$) design (within heat pipe)	Could result in localized zone of enhanced water-rock interaction and chemical transport
Conductive heating	Heat transfer within low-permeability and unsaturated portions of geothermal systems	Nearly ubiquitous: examples include hot dry rock resources, upper portions of San Vicente (El Salvador), Amatitlan (Guatemala)	Main mechanism of heat transfer at Yucca Mountain (unsaturated conditions)	Heating leads to more rapid chemical reactions. Thermal expansion of rocks could alter fracture permeability
Fracture-dominated fluid flow	Fluid flow in fractured reservoir rocks with low matrix permeability	Silangkitang (Indonesia), Dixie Valley (Nevada), Los Azufres (Mexico)	Main mechanism for fluid flow within welded ash flow tuffs at Yucca Mountain	Could permit rapid movement of fluids along fast flow paths (evidenced by bomb-pulse tritium)
Chemical transport	Advective and diffusive transport of dissolved constituents in fluids. Tracer tests used to determine fluid flow paths and rates.	Ubiquitous. Well-documented tracer tests for many geothermal systems, including The Geysers (California), Dixie Valley (Nevada), Coso (California), Awibengkok (Indonesia)	Advective transport within fractures, and advective and diffusive transport between fractures and matrix	Potential mechanism for movement of radioactive waste materials from repository
Boiling	Development of two-phase and steam zones in geothermal systems due to depressurization and heating	Occurs in most high-temperature liquid-dominated geothermal systems with production, e.g., Awibengkok (Indonesia), Coso (California), and occurs naturally in steam-dominated systems, e.g., The Geysers (California), Karaha-Telaga-Bodas (Indonesia).	Would only occur in high-temperature design near drift walls for limited time	Would create dryout zone around drift for high-temperature design, and could lead to development of heat pipe. Fracture permeability could be modified by precipitation caused by boiling.
Dryout	Occurs during transformation from liquid-dominated to steam-dominated geothermal system	Documented for The Geysers (California), Karaha-Telaga-Bodas (Indonesia)	Would only occur in high-temperature operating mode near drift walls for limited time	Dryout zone would prohibit seepage into drift for early stages of high-temperature operating mode. Would lead to precipitation of dissolved solids in area that could be redissolved as cooling and rewetting occurred.

Table 11.2-1. THC Processes in Geothermal Systems and Their Applicability to Yucca Mountain (Cont.)

THC process	Geothermal system component	Geothermal examples	Applicability to Yucca Mountain	Potential impact to repository performance
Condensation	Occurs during transformation from liquid-dominated to steam-dominated geothermal system, and in upper levels of geothermal systems where rising vapor contacts cooler meteoric waters	Observed in many geothermal systems where rising gas and steam is cooled and mixes with near-surface meteoric fluids, resulting in development of bicarbonate and acid-sulfate springs. Documented for Yellowstone (Wyoming), Wairakei (New Zealand), Waiotapu (New Zealand)	Would mainly occur in high-temperature design above drift areas for limited time; can also occur in low-temperature design, but at a reduced level	Condensation above drift could lead to recycling of fluids, thus resulting in a higher volume of fluids passing through near-field area. This could also result in localized zones of near-saturation conditions and increase water-rock interaction. Condensation could also take place in the drift, resulting in dripping on waste packages.
Mineral dissolution	Occurs typically in condensation zones, or where acid fluids are present	Difficult to document, but observed at The Geysers (California) and Karaha-Telaga-Bodas (Indonesia)	Would occur primarily where condensation occurs	Mineral dissolution associated with condensation zone could lead to local increases in porosity and permeability.
Mineral alteration and precipitation	Occurs in numerous portions of geothermal systems, especially in zones with abundant fluid flow that have undergone heating	Ubiquitous. Degree and type of mineralization depends on rock and fluid compositions, water-rock ratios, and temperature. Boiling can result in significant mineralization. Alteration mineralogy well-characterized at Wairakei (New Zealand), Salton Sea (California), Silangkitang (Indonesia), Krafla (Iceland)	Alteration and precipitation likely to be confined to near-field environment, where boiling and increased fluid flux occur. These effects may be negligible for low-temperature design.	Alteration could lead to changed sorption properties (zeolite and clay formation). Precipitation of silica minerals and calcite in fractures could locally reduce permeability, or lead to focussed flow within a few larger fractures.

Source: Simmons 2002 [157578], SN-LBNL-SCI-108-V2, pp. 14–15.